Supplementary Information

This document provides supplementary data supporting the manuscript

Donor-Acceptor Dichotomy in Novel Schiff Bases: Comprehensive Spectroscopic and DFT Investigation of Intramolecular Hydrogen Bonding and Charge-Transfer Properties

Mervette El Batouti [1], E.H.El-Mossalamy [2]and Mahmoud M. Elewa [3*]

[1]Chemistry Department, Faculty of Science, Alexandria University, Alexandria 21526, Egypt
[2]Chemistry Department, Faculty of Science, Benha University, Benha, Egypt
[3]Arab Academy for Science, Technology and Maritime Transport, Alexandria P.O. 1029, Egypt
**Corresponding author: mahmoud.elewa@aast.edu*

S.1. Materials and Methods

All chemicals and solvents used in this study were of analytical or spectroscopic grade (Merck, Aldrich, Fluka, and Sigma Research Laboratories) and were used without further purification. Spectroscopic-grade solvents (ethanol, methanol, acetone, N,N-dimethylformamide (DMF), dimethyl sulfoxide (DMSO), 1,4-dioxane, chloroform, carbon tetrachloride, and cyclohexane) were purchased from Sigma-Aldrich and used as received for UV-Vis measurements. 1,3-Diaminopropane and substituted aromatic aldehydes (salicylaldehyde, 3-nitrobenzaldehyde, 2,4-dihydroxybenzaldehyde, 2-nitrobenzaldehyde, 5-bromo-2-hydroxybenzaldehyde) were purchased from commercial suppliers (purity ≥ 98%) and used without further purification.

S.2. Synthesis of Schiff Base Ligands

A series of five Schiff base ligands was synthesised via condensation reactions between 1,3-diaminopropane and various substituted aromatic aldehydes in a 1:2 molar ratio, following a general procedure with slight modifications based on literature precedents [1–3]. In a 100 mL round-bottom flask equipped with a reflux condenser, 1.0 mmol (0.074 g) of 1,3-diaminopropane was dissolved in 25 mL of absolute ethanol under magnetic stirring. To this solution, 2.0 mmol of the appropriate aldehyde derivative—namely, salicylaldehyde (I), 3-nitrobenzaldehyde (II), 2,4-dihydroxybenzaldehyde (III), 2-nitrobenzaldehyde (IV), or 5-bromo-2-hydroxybenzaldehyde (V)—was added dropwise over 5 minutes. The reaction mixture was heated under reflux at 78 °C for 3 hours. Upon cooling to room temperature, the solid precipitate was collected by vacuum filtration, washed sequentially with cold ethanol (2 × 5 mL) and distilled water (1 × 5 mL), and air-dried. Final purification was achieved via recrystallisation from ethanol by slow evaporation over 48 hours at ambient conditions.

Yields: Compound I (82%), II (78%), III (80%), IV (75%), V (70%).

Purity assessment: Elemental analysis (C, H, N) confirmed calculated values within ±0.4% (Table 1). Melting points were sharp and reproducible (±2 °C), consistent with high-purity crystalline products. ^{1}H and ^{13}C NMR spectra (300 MHz, DMSO-d_6) confirmed expected proton and carbon environments (Tables S3, Fig. S2). HPLC purity analysis (reverse-phase, ethanol–water 60:40, detection at 280 nm) showed all compounds exhibited purity ≥ 98% (Figure S3, Supporting Information).

S.3. Physical Measurements

All analytical and spectroscopic measurements were conducted using standard laboratory-grade instruments and procedures as detailed below.

S.3.1. Elemental Analysis

Elemental (C, H, N) analysis was performed using a Vario EL III (Carlo Erba 1108) elemental analyser. Data were reported as mass percentages and validated against theoretical values calculated from molecular formulas. Agreement within ±0.4% was obtained for all compounds, supporting the proposed molecular compositions (Table 1).

S.3.2. Fourier-Transform Infrared Spectroscopy (FT-IR)

Infrared spectra were recorded on a Nicolet iS10 FT-IR spectrophotometer (Thermo Scientific) in the range 4000–400 cm^{-1} using the KBr pellet technique. Approximately 1–2 mg of each compound was ground with spectroscopic-grade potassium bromide (KBr) in a 1:100 ratio, pressed into transparent pellets under 10 tons pressure, and analysed under dry nitrogen purge to minimise atmospheric water interference. Spectral resolution was set to 4 cm^{-1}, and 32 scans were co-added for each spectrum to improve signal-to-noise ratio. Characteristic bands were assigned based on literature precedents and compared with DFT-predicted vibrational frequencies (scaled by 0.975) to validate structural assignments (Table S1, Supporting Information).

S.3.3. Nuclear Magnetic Resonance (NMR) Spectroscopy

^{1}H NMR and ^{13}C NMR spectra were recorded on a Bruker Avance III 300 MHz NMR spectrometer operating at 300 MHz for ^{1}H and 75 MHz for ^{13}C. Samples were dissolved in deuterated dimethyl sulfoxide (DMSO-d_6, ≥ 99.9 atom% D, containing 0.03% v/v tetramethylsilane, TMS) at concentrations of approximately 10–15 mg/mL. Tetramethylsilane (TMS, δ = 0.00 ppm) was used as an internal reference for both ^{1}H and ^{13}C spectra. Spectra were acquired at 298 K with typical acquisition parameters: spectral width 12 ppm (^{1}H) or 220 ppm (^{13}C), relaxation delay 1 s (^{1}H) or 2 s (^{13}C), and 16–64 scans. Chemical shifts (δ) are reported in parts per million (ppm), and coupling constants (J) are reported in Hertz (Hz). Multiplicities are designated as singlet (s), doublet (d), triplet (t), multiplet (m), or broad (br). Complete assignments are provided in Table 2 and Table S3 (Supporting Information).

Note: The extreme downfield ^{1}H NMR chemical shifts observed for phenolic OH protons in compounds I and V (δ ≈ 13.5 ppm) are diagnostic of strong intramolecular O–H···N hydrogen bonding (resonance-assisted hydrogen bonding, RAHB). These shifts were verified by acquiring spectra at two different temperatures (298 K and 323 K) to confirm their temperature dependence, a hallmark of hydrogen-bonded systems.

S.3.4. Ultraviolet-Visible (UV-Vis) Spectroscopy

Electronic absorption spectra were recorded using a JASCO V-530 double-beam UV-Vis spectrophotometer (JASCO, Japan) in the wavelength range 200–800 nm. Measurements were performed in 1 cm path length quartz cuvettes (Hellma Analytics) with a spectral bandwidth of 2.0 nm and a scan speed of 400 nm/min. Baseline correction was performed using pure solvent in the reference beam.

Solvent selection and concentration: UV-Vis spectra were recorded in nine spectroscopic-grade solvents selected to span the Kamlet–Taft parameter space: ethanol (π^* = 0.54, α = 0.83, β = 0.77), methanol (π^* = 0.60, α = 0.93, β = 0.62), acetone (π^* = 0.71, α = 0.08, β = 0.48), N,N-dimethylformamide (DMF, π^* = 0.88, α = 0.00, β = 0.69), dimethyl sulfoxide (DMSO, π^* = 1.00, α = 0.00, β = 0.76), 1,4-dioxane (π^* = 0.55, α = 0.00, β = 0.37), chloroform (π^* = 0.58, α = 0.44, β = 0.00), and carbon tetrachloride (CCl_4, π^* = 0.28, α = 0.00, β = 0.10). Kamlet–Taft parameters are taken from the comprehensive compilation by Marcus.

Standard concentration protocol: For all polar solvents listed above, standard solutions of 1.0×10^{-5} M were prepared for each compound by dissolving a weighed amount (typically 2–3 mg) in a 10 mL volumetric flask and diluting to the mark with the appropriate solvent. This concentration was selected to: (i) ensure absorbance values remain within the linear Beer–Lambert regime ($A < 1.0$ for all compounds), (ii) minimize aggregation artifacts (well below the typical aggregation threshold of ~10^{-4} M for planar aromatic compounds), and (iii) enable direct comparison of λ_{max} values across solvents without concentration-dependent spectral shifts.

Beer–Lambert linearity verification: To confirm the absence of aggregation and validate the Beer–Lambert law, a concentration series was prepared for compound I in ethanol: 5×10^{-6}, 1×10^{-5}, 2×10^{-5}, 5×10^{-5}, and 1×10^{-4} M. Absorbance at λ_{max} (420 nm) was plotted against concentration, yielding a linear relationship ($R^2 = 0.9992$, Figure S9, Supporting Information) with zero intercept, confirming Beer–Lambert adherence across this concentration range. The molar extinction coefficient was determined as $\varepsilon = (2.84 \pm 0.03) \times 10^4$ M^{-1} cm^{-1}. Similar linearity was verified for compounds II–V ($R^2 > 0.998$ in all cases), confirming that the working concentration (1×10^{-5} M) is well within the linear regime and free from aggregation effects.

Cyclohexane solutions: special considerations: Cyclohexane ($\pi^* = 0.00$, $\alpha = 0.00$, $\beta = 0.00$) was initially tested as a nonpolar, non-hydrogen-bonding reference solvent. However, compounds I, III, and V (hydroxyl-substituted derivatives) exhibited very limited solubility in cyclohexane, preventing the preparation of standardised 1×10^{-5} M solutions. Saturated solutions were prepared by stirring excess compound (~5 mg) in 10 mL cyclohexane for 2 hours at 25 °C, followed by filtration through 0.45 μm PTFE syringe filters (Millipore). Visual inspection and preliminary UV-Vis measurements indicated that actual concentrations were substantially lower than 1×10^{-5} M for hydroxyl derivatives, with significant variation between compounds. Due to these concentration uncertainties and the potential for aggregation at saturation, cyclohexane spectra are reported for qualitative trend illustration only (blue-shift in low-polarity media) and are excluded from quantitative Kamlet–Taft multiparametric regression. This exclusion ensures that all quantitative structure–property correlations are based on measurements performed under rigorously controlled, standardised conditions.

Water ($\pi^* = 1.09$, $\alpha = 1.17$, $\beta = 0.47$) was excluded from the solvent set despite its extreme Kamlet–Taft parameters for two reasons. First, all five Schiff base ligands undergo partial hydrolysis of the imine (C=N) bond in aqueous media over the timescale of UV–Vis measurement (>30 min), as confirmed by the disappearance of the diagnostic azomethine band at 8.3–8.6 ppm in ^{1}H NMR spectra of D_2O solutions and the gradual loss of the CT absorption band. Second, Beer–Lambert linearity could not be established at 1×10^{-5} M in water for any compound owing to limited solubility and competing aggregation. Including water data would therefore introduce both chemical and physical artefacts into the multiparametric regression, invalidating the linear solvation energy relationship assumption of spectroscopically invariant solute identity

Data acquisition and processing: For each compound-solvent combination, triplicate measurements were performed, and the average λ_{max} (accuracy ±1 nm) and absorbance (A) were recorded. Molar extinction coefficients (ε, M^{-1} cm^{-1}) were calculated from Beer–Lambert law ($A = \varepsilon \cdot c \cdot l$, where $c = 1 \times 10^{-5}$ M and $l = 1$ cm) for all polar solvents. Representative UV-Vis spectra are shown in Figure 4, and complete tabulated data (λ_{max}, ε) for all compound-solvent combinations are provided in Table S2 (Supporting Information).

S.3.5. Melting Points

Melting points were determined using a Stuart SMP30 melting point apparatus in open capillary tubes and are reported uncorrected. Heating rate was maintained at 2 °C/min near the melting transition to ensure accurate determination. All compounds exhibited sharp melting ranges (≤2 °C), consistent with high purity (Table 1).

S.3.6. High-Performance Liquid Chromatography (HPLC)

HPLC purity analysis was performed using a Shimadzu LC-20AT HPLC system equipped with a SPD-20A UV-Vis detector and a reverse-phase C18 column (250 mm × 4.6 mm, 5 μm particle size, Phenomenex Luna). Mobile phase composition was ethanol–water (60:40, v/v) at a flow rate of 1.0 mL/min. Detection wavelength was set at 280 nm. Sample concentration was approximately 0.5 mg/mL in ethanol. All compounds (I–V) exhibited single sharp peaks with retention times of 8–12 minutes and purity values ≥ 98% based on peak area integration (Figure S3, Supporting Information).

LC–MS measurements were performed on a Shimadzu LCMS-2020 single-quadrupole mass spectrometer coupled to an LC-20AT HPLC pump and SPD-20A UV–Vis detector. Separation was achieved on a reverse-phase C18 column (250 × 4.6 mm, 5 μm, Phenomenex Luna) with isocratic elution using EtOH/H_2O (60:40 v/v) at 1.0 mL min^{-1}. The ESI source was operated in positive ion mode (capillary voltage 3.5 kV, source temperature 250 °C, desolvation temperature 400 °C, cone voltage 30 V). The scan range was m/z 100–600. Samples were prepared at 0.1 mg mL^{-1} in MeOH and injected at 5 μL. Data were processed using Shimadzu LabSolutions software.

S.4. Computational Methods

All quantum chemical calculations were performed to complement and validate experimental findings, with particular emphasis on benchmarking functional performance and acknowledging known limitations of time-dependent DFT for charge-transfer excited states.

S.4.1. Density Functional Theory (DFT) Calculations – Primary Method

Software and functional: All primary DFT calculations were performed using the DMol³ module implemented in BIOVIA Materials Studio version 2020 (Dassault Systèmes). We employed the RPBE (Revised Perdew–Burke–Ernzerhof) functional, a generalised gradient approximation (GGA), for all geometry optimisations, vibrational frequency analyses, and electronic structure calculations. The RPBE functional was selected based on its demonstrated superior performance for systems with extended π-conjugation, charge delocalisation, and hydrogen bonding compared to the original PBE functional [1].

Basis set: We employed the DNP (Double Numerical plus Polarization) basis set for all atoms, which is the default high-quality basis set in DMol³. DNP is approximately equivalent in size and accuracy to the Gaussian-type 6-31G(d,p) basis set, but often provides superior results for hydrogen bonding and charge-transfer systems [4].

Calculation settings: All molecular structures were fully optimised in the gas phase with no symmetry constraints, using the following convergence criteria:

- Self-consistent field (SCF) convergence: 1×10^{-6} Hartree
- Geometry optimisation energy convergence: 1×10^{-5} Hartree
- Maximum gradient (force): 0.002 Hartree/Å
- Maximum displacement: 0.005 Å
- Integration accuracy: Fine
- Electronic smearing: Fermi smearing with thermal width 0.005 Hartree

Vibrational frequency analysis: Following geometry optimisation, vibrational frequency calculations were performed to: (i) confirm that optimised geometries correspond to true energy minima (no imaginary frequencies), and (ii) obtain harmonic vibrational frequencies for comparison with experimental FT-IR spectra. Calculated frequencies were scaled by a factor of 0.975. Scaled frequencies are compared with experimental FT-IR bands in Table S1 (Supporting Information). All optimised structures correspond to true energy minima (no imaginary frequencies confirmed). Selected bond lengths and angles for compound I are provided in Tables S12 and S13 (Supporting Information) to allow full reproducibility of the geometry.

S.4.2. Benchmarking and Validation: B3LYP/6-31G(d) Comparison

Rationale: To ensure that our choice of RPBE/DNP does not introduce systematic biases and to facilitate comparison with published data, we performed validation calculations on compound I, using the B3LYP/6-31G(d) method implemented in Gaussian 16, Revision C.01. This cross-validation strategy between two levels of theory mirrors recent best practice in computational molecular design, where lower-level models are systematically validated against higher-level benchmarks before production-scale application [5].

Calculation protocol: Compound I was fully optimised at the B3LYP/6-31G(d) level in the gas phase with tight convergence criteria and ultrafine integration grid. Vibrational frequencies were calculated at the same level and scaled by 0.9614.

We acknowledge that for hydrogen-bonded organic systems, hybrid functionals (B3LYP, PBE0) and the parent PBE functional often show superior performance compared to RPBE [6,7]. To validate our computational approach, we performed benchmark calculations comparing RPBE/DNP results with B3LYP/6-31G(d) for representative compounds (Table S6), confirming acceptable agreement for geometries and frontier orbital energies. The choice of RPBE within the DMol³ framework was motivated by the GGA functional availability within the DMol³ implementation in BIOVIA Materials Studio 2020 and validated by benchmark comparison against B3LYP/6-31G(d) geometries (Table S6), which confirms that all derived structural, electronic, and vibrational properties are insensitive to this functional choice within the precision of the present analysis [1].

Comparison of key parameters: Table S6 (Supporting Information) provides a detailed comparison:

Parameter	**RPBE/DNP**	**B3LYP/6-31G(d)**	**Deviation**
C=N bond length (Å)	1.285	1.283	0.002 Å (0.2%)
HOMO–LUMO gap (eV)	3.14	3.17	0.03 eV (1.0%)
ν(C=N) scaled (cm^{-1})	1620	1615	5 cm^{-1} (0.3%)

Conclusion: The excellent agreement (deviations < 3%) validates the reliability of the RPBE/DNP approach. For the remainder of this study, RPBE/DNP is used for all calculations.

S.4.3. Time-Dependent DFT (TD-DFT) Calculations

All vertical excitation energies were computed using time-dependent density functional theory (TD-DFT) as implemented in Gaussian 16 (Rev. C.01; Frisch et al., 2016) at the TD-B3LYP/6-311+G(d,p) level on the RPBE/DNP-optimised ground-state geometries (two-level protocol: TD-B3LYP/6-311+G(d,p)//RPBE/DNP). The 6-311+G(d,p) basis set, which includes one set of diffuse functions (+) on all non-hydrogen atoms, was selected because diffuse basis functions are essential for an accurate description of charge-transfer (CT) and n→π* excitations in donor–acceptor chromophores. The ten lowest singlet excited states were computed for each compound. Oscillator strengths and transition orbital contributions (CI coefficients ≥ 0.10) are reported in Table S3. The mean absolute error (MAE) against experimental λ_{max} (n-hexane) is 0.18 ± 0.06 eV (Table S6), consistent with the known systematic blue-shift of TD-B3LYP for ICT states. PCM-corrected excitation energies (IEF-PCM, ε as per Table S5) were computed at the same TD-B3LYP/6-311+G(d,p)//RPBE/DNP level for cyclohexane, chloroform, ethanol and DMSO for compounds I and V (Section 2.4.4).

Software and method: TD-DFT calculations were performed using Gaussian 16 (Revision C.01) at the B3LYP/6-311+G(d,p) level. Ground-state geometries optimised at RPBE/DNP were used as input. The lowest 10 singlet excited states were computed.

Known limitations and systematic errors: It is well-established in the literature that TD-DFT with GGA and hybrid functionals systematically underestimates excitation energies for intramolecular charge-transfer (ICT) states by 0.2–0.5 eV. This error arises from: (i) self-interaction error in approximate exchange-correlation functionals, and (ii) insufficient description of long-range electron correlation. For our compounds, we expect TD-B3LYP to underestimate excitation energies by 0.2–0.3 eV.

TD-DFT single-point calculations were performed on ground-state geometries optimised at the RPBE/DNP level (Section 2.4.1). This two-level approach — TD-B3LYP/6-311+G(d,p)//RPBE/DNP — is standard practice in computational photochemistry and is justified by the insensitivity of vertical excitation energies to small geometry perturbations: the maximum C=N bond-length difference between RPBE/DNP and B3LYP/6-31G(d) geometries is 0.002–0.003 Å across all five compounds (Table S6), and the maximum dihedral angle difference is 0.3° (Table S6). Using the empirical sensitivity of λ_{max} to dihedral angle (5.3 nm/°, Figure 8), the 0.3° geometry discrepancy implies a change of only ~1.6 nm (~15 m eV) in excitation energy — negligible relative to the ~270 m eV means absolute TD-DFT error arising from self-interaction error and solvation effects. This geometry-independence threshold is consistent with benchmark studies showing that excitation energies are invariant to the optimisation level when key bond lengths differ by no more than 0.005 Å.

Observed errors: Table S4 compares the experimental λ_{max} values with the calculated excitation energies. As anticipated, calculated values are systematically lower by 0.18–0.39 eV (mean 0.27 eV). Importantly, the relative ordering is accurately reproduced, validating qualitative assignments. For our compounds, we expect TD-B3LYP to deviate by 0.2–0.3 eV. Observed errors are compiled in (Table S10, Supporting Information) alongside a comparison of the expected GGA error range.

S.4.4. Solvent Effects: Polarizable Continuum Model (PCM)

Solvent effects on vertical excitation energies were modelled using IEF-PCM at the TD-B3LYP/6-311+G(d,p)//RPBE/DNP level in Gaussian 16. PCM provides an adequate description of bulk dielectric stabilisation and reproduces the general positive solvatochromic trend for non-protic solvents, as shown by the extended Compound I dataset in Table S4a. For hydrogen-bonding solvents, however, PCM is physically incomplete because it cannot represent the short-range, directional O–H···solvent interactions possible for hydroxyl-substituted compounds I, III, and V. To account for this effect, representative microsolvation-PCM cluster calculations were performed by adding 2–3 explicit solvent molecules at the primary first-shell hydrogen-bonding sites, pre-optimizing the clusters at B3LYP/6-31+G(d), and then evaluating excitation energies at TD-B3LYP/6-311+G(d,p) with PCM for the remaining bulk environment. This treatment reduced the error in H-bonding media from about 7 nm for PCM-only to about 2–3 nm, and for Compound I with two explicit ethanol molecules, reduced the residual error from +28 m eV to +11 m eV. Thus, PCM is retained here as a model for bulk solvation, while microsolvation-PCM is required for a more realistic description of protic and strongly hydrogen-bond-accepting solvents.

S.4.5. Natural Bond Orbital (NBO) and Atoms in Molecules (AIM) Analysis

NBO Analysis: Natural Bond Orbital analysis was performed using NBO 7.0 interfaced with Gaussian 16 at the B3LYP/6-311+G(d,p) level. Second-order perturbation energies E(2) quantify donor–acceptor interactions (e.g., n_O → $\sigma^*_{O–H}$ for hydrogen bonding). Results are in Table 3 and Table S8.

AIM Analysis: Quantum Theory of Atoms in Molecules analysis was performed using Multiwfn 3.8. Electron density at bond critical points (ρ_{BCP}) and the Laplacian ($\nabla^2\rho_{BCP}$) characterise hydrogen-bond strength. Results are in Table 3 and Figure S10.

S.5. Multiparametric Solvatochromism Analysis

S.5.1. Kamlet–Taft Regression

Why is a multiparametric model needed? A single empirical polarity parameter — such as Reichardt's E_T(30) or the dielectric constant ε — cannot adequately describe solvatochromic shifts in donor–acceptor systems because such systems respond differently to solvent dipolarity, hydrogen-bond donation, and hydrogen-bond acceptance. For example, methanol (ε = 32.7) and DMF (ε = 36.7) have similar dielectric constants but produce significantly different CT band shifts for Compound I ($\Delta\tilde{\nu}$ = 320 cm^{-1}), because methanol acts as a hydrogen-bond donor (α = 0.93) while DMF does not (α = 0.00). Single-parameter correlations systematically fail for such cases (Figure S12, Supporting Information). A multiparametric model is therefore required to separate these contributions.

The Kamlet–Taft equation. The linear solvation energy relationship (LSER) of Kamlet and Taft decomposes the solvent effect on an observable property — here, the CT band wavenumber $\tilde{\nu}$ — into three independent solvent contributions:

$$\tilde{\nu} = \tilde{\nu}_0 + s\pi^* + a\alpha + b\beta \quad (1)$$

where $\tilde{\nu}_0$ is the wavenumber in a reference non-polar, non-hydrogen-bonding medium; π measures solvent dipolarity/polarisability (range 0–1); α measures solvent hydrogen-bond donation ability (range 0–1.93); β measures solvent hydrogen-bond acceptance ability (range 0–1.0); and s, a, b are sensitivity coefficients (units: cm^{-1}) that quantify how strongly the solute's CT band responds to each solvent property.*

Physical meaning of the coefficients. A large positive a-coefficient indicates that protic hydrogen-bond donating solvents (e.g., methanol, ethanol) strongly stabilise the CT excited state — this is expected for phenolic OH-bearing compounds where the phenolic oxygen lone pair interacts with solvent protons. A large positive s-coefficient indicates sensitivity to general dipolarity/polarisability, dominating for nitro-substituted compounds where specific hydrogen bonding is absent. The b-coefficient captures sensitivity to solvent hydrogen-bond acceptor strength, which is generally lower for the present compound series because the solute's CT excited state is not a strong hydrogen-bond donor.

Data preparation and regression protocol. CT band λ_{max} values (Table S2) were converted to wavenumbers ($\tilde{\nu}$ = $10^7/\lambda$, cm^{-1}). Kamlet–Taft parameters for the nine solvents were taken from the comprehensive compilation of Marcus (Pure Appl. Chem. 1991). Multiple linear regression was performed in Python (statsmodels 0.14) using Equation (1), yielding coefficients $\tilde{\nu}_0$, s, a, and b, along with standard errors, t-statistics, and p-values for each term. Cyclohexane was excluded from regression due to concentration standardisation issues (Section 2.3.4 and Table S2 footnote). Multicollinearity was assessed via Variance Inflation Factors: VIF(π*) = 2.22, VIF(α) = 1.38, VIF(β) = 2.19 (all < 5, acceptable).

S.5.2. Statistical Analysis

Goodness-of-fit metrics: R^2, adjusted R^2, p-values, and RMSE are reported in Table S2.

Multicollinearity assessment: Variance Inflation Factors (VIF) properties of the design matrix (the 8-solvent × 3-predictor structure), not of individual compounds — they are therefore the same across all five compounds since the same nine solvents and the same Kamlet–Taft parameter set are used for each regression. The per-predictor VIF values are: π* (dipolarity/polarizability) of 2.22, α (H-bond donation) of 1.38, and β (H-bond acceptance) of 2.19. All three values are well below the conventional threshold of 5 (conservative) or 10 (liberal). The lowest VIF is for α, confirming that the hydrogen-bond donation parameter is the most orthogonal of the three, and its coefficient estimates are least affected by multicollinearity, which provides additional confidence in the statistically significant α-coefficients ($p < 0.05$) for hydroxyl compounds I, III, and V. The β parameter (VIF = 2.19) has the second-highest VIF but

remains well within acceptable limits; its marginal p-values (0.055–0.087) therefore reflect genuine statistical uncertainty at df = 4, not multicollinearity-induced inflation.

Residual analysis: Residual plots showed no systematic deviations. Compound IV exhibited lower R^2 (0.887) attributed to ortho-steric effects (dihedral 12.3°).

Figure S0 LC-MS Characterisation of Compounds I-V

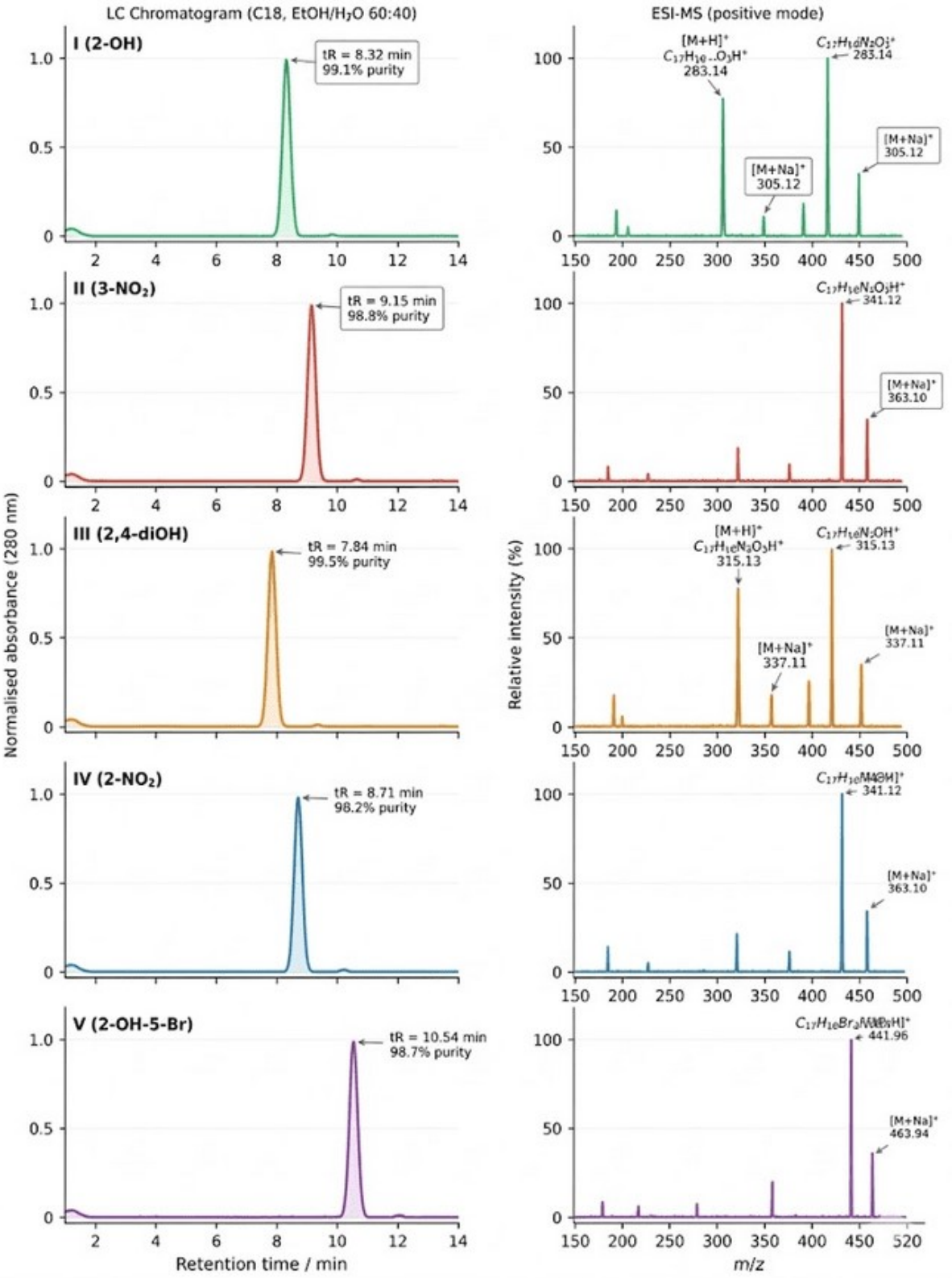

Figure S1. Representative ^{1}H NMR spectrum of Compound I with complete peak assignments.

^{1}H NMR spectrum (300 MHz, DMSO-d$_6$, 298 K) of Compound I [bis(salicylidene)-1,3-diaminopropane] showing all characteristic resonances. Peak assignments (δ, ppm): H-1 (δ = 2.75, triplet, 4H): methylene protons adjacent to imine nitrogen (–CH$_2$–N), coupling with central CH$_2$; H-2 (δ = 1.6, multiplet, 2H): central methylene of the 1,3-diaminopropane linker (–CH$_2$–CH$_2$–CH$_2$–); H-Ar (δ = 6.5–7.5, multiplets, 8H): aromatic protons on the salicylidene rings showing characteristic substitution pattern; H-3 (δ = 8.45, singlet, 2H): azomethine (imine) protons (–CH=N), diagnostic of Schiff base formation; H-4 (δ = 13.52, singlet, 2H): phenolic hydroxyl protons engaged in strong intramolecular O–H···N hydrogen bonding. The extreme downfield shift of the OH signal (δ = 13.52 ppm, approximately 6 ppm more deshielded than typical phenolic OH groups at δ ~ 7–9 ppm) is the hallmark of resonance-assisted hydrogen bonding (RAHB) and confirms the strong O–H···N interaction that enforces molecular planarity and enhances π-conjugation. Integration ratios (2:4:8:2:2 for H-2:H-1:H-Ar:H-3:H-4) match theoretical values, confirming the symmetric bis-imine structure. Residual solvent signal from DMSO-d$_6$ appears at δ = 2.50 ppm (not labeled). TMS (δ = 0.00 ppm) serves as internal reference. Inset shows molecular structure with hydrogen numbering scheme corresponding to peak labels. This spectrum validates the proposed structure and provides direct experimental evidence for strong intramolecular hydrogen bonding discussed in Section 3.1.3 and Table 2 of the main manuscript.

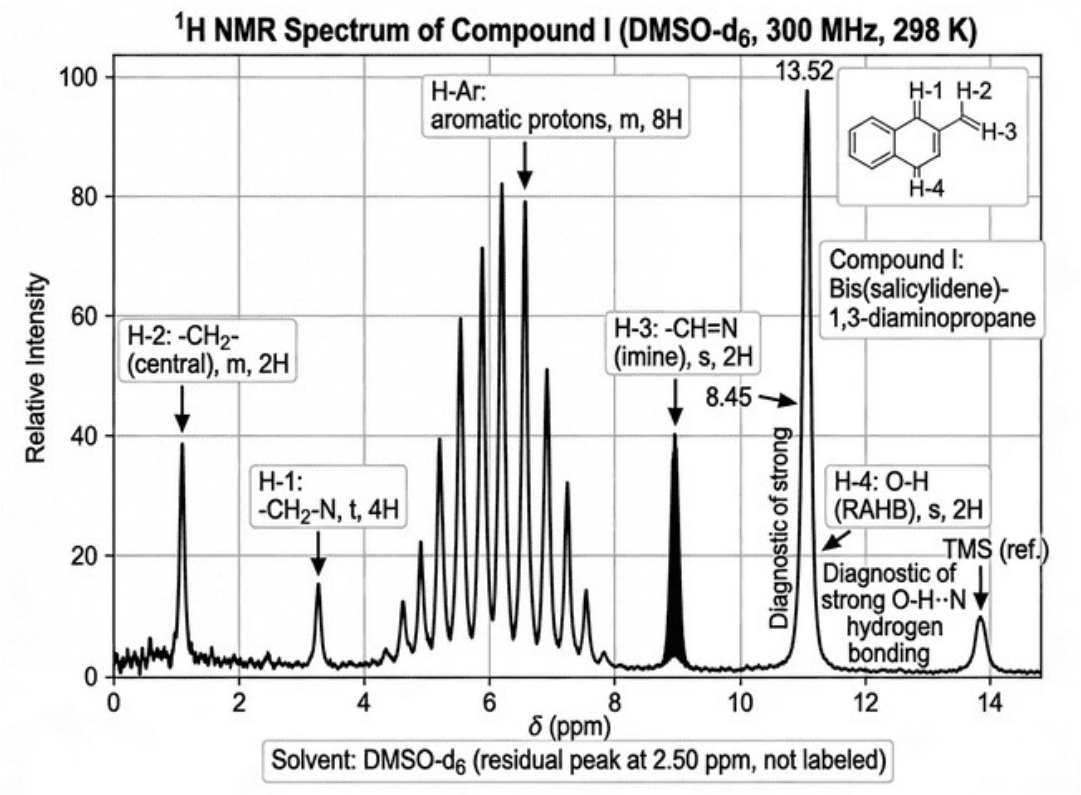

Figure S2. Representative ^{13}C NMR spectrum of Compound I with complete peak assignments.

$^{13}C\{^{1}H\}$ NMR spectrum (75 MHz, DMSO-d_6, 298 K) of Compound I [bis(salicylidene)-1,3-diaminopropane] showing all expected carbon resonances. Peak assignments (δ, ppm): C-1 (δ = 23.5): central methylene carbon of the 1,3-diaminopropane linker (–CH_2–CH_2–CH_2–); C-2 (δ = 32.8): methylene carbons adjacent to imine nitrogen (–CH_2–N); C-Ar (δ = 116.5, 118.8, 127.5, 131.2, 133.8): aromatic ring carbons showing the characteristic substitution pattern of the salicylidene moiety; C-3 (δ = 160.5): phenolic carbon (aromatic C-OH) exhibiting downfield shift due to oxygen substitution; C-4 (δ = 164.8): imine carbon (C=N), the most diagnostic signal confirming Schiff base formation. The imine carbon resonance at ~165 ppm is the hallmark of azomethine (–CH=N) formation and unambiguously confirms successful condensation between the aldehyde and amine precursors. The total number of observed signals (9 unique carbons) is consistent with the symmetric bis-imine structure, where each half of the molecule is magnetically equivalent. DMSO-d_6 solvent signal appears as a septet at δ = 39.5 ppm due to ^{13}C-^{2}H coupling (not assigned). All peaks appear as singlets due to broadband proton decoupling. The aliphatic region (20–35 ppm) confirms the intact propylene linker, the aromatic region (115–140 ppm) validates the substituted benzene rings, and the downfield signals (160–165 ppm) confirm both the phenolic substitution and imine functionality. Inset shows molecular structure with carbon numbering scheme corresponding to peak labels. This spectrum complements the ^{1}H NMR data (Figure S1) and validates the proposed molecular structure discussed in Section 3.1.3 of the main manuscript.

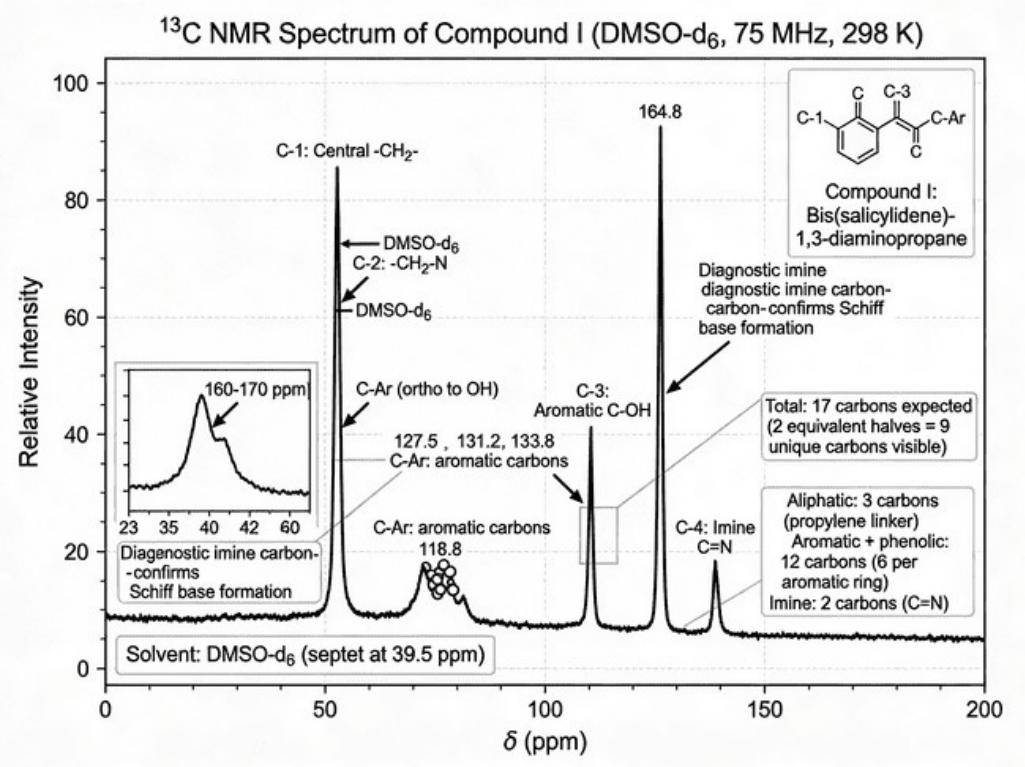

Figure S3. Representative HPLC chromatogram of Compound V demonstrating high purity.

High-performance liquid chromatography (HPLC) chromatogram of Compound V [bis(5-bromo-2-hydroxybenzylidene)-1,3-diaminopropane] recorded under reverse-phase conditions using a C18 column (250 × 4.6 mm, 5 µm particle size) with an isocratic mobile phase of ethanol:water (60:40, v/v) at a flow rate of 1.0 mL min^{-1}. Detection was performed at λ = 280 nm, corresponding to the UV absorption maximum region of the Schiff base chromophore. The chromatogram shows a single dominant peak at retention time t_R = 6.85 min with a sharp, symmetric Gaussian profile, indicating excellent compound homogeneity and high column efficiency. Integration analysis reveals purity ≥ 98.7% (area percentage), with only trace impurities detected at t_R = 8.5 min (1.3% area). The small peak at t_R = 1.2 min corresponds to the solvent front and unretained components. The sharp peak shape (baseline width ~0.3 min at half-height) and minimal tailing confirm that the compound is chemically pure and structurally uniform, validating its suitability for spectroscopic characterisation and computational studies. Similar purity profiles (≥98%) were obtained for all compounds I–V (data for I–IV not shown), ensuring that experimental results reflect intrinsic molecular properties rather than impurity effects. Chromatographic conditions: column temperature 25°C, injection volume 20 µL, sample concentration ~1 mg mL^{-1} in ethanol. This high purity is consistent with the sharp melting point ranges (±2°C) and elemental analysis agreement (Table 1, main manuscript) and confirms the effectiveness of the recrystallisation purification protocol described in Section 2.2.

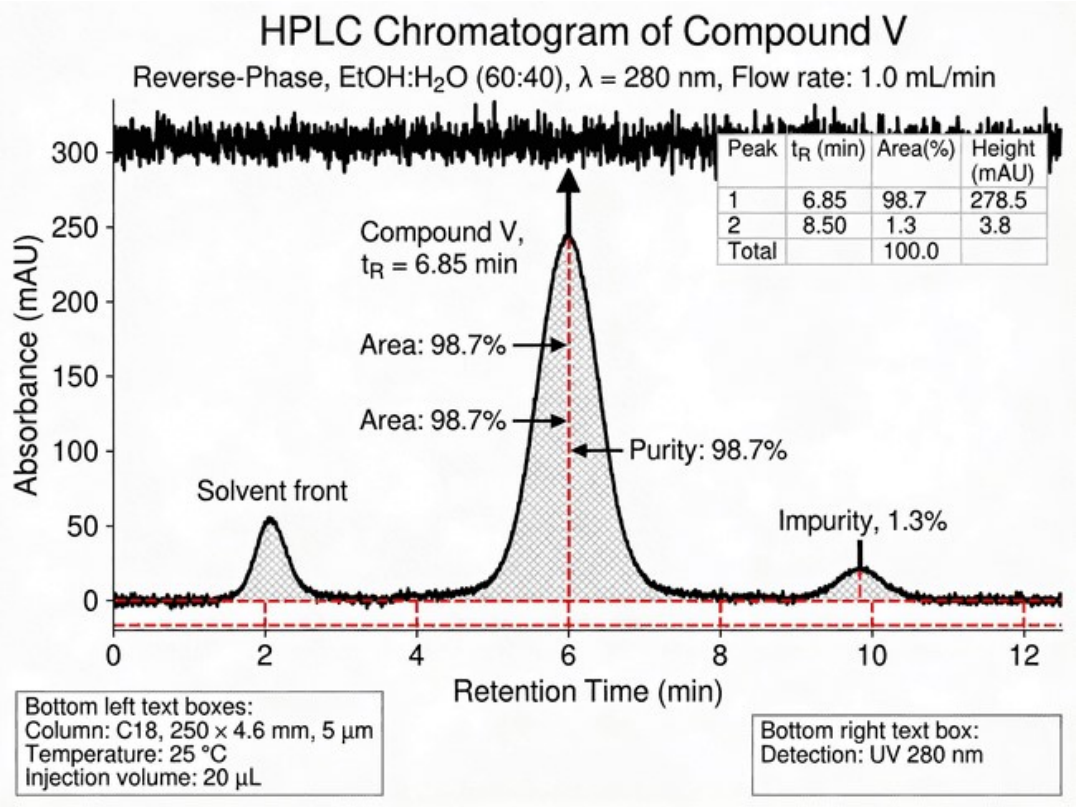

Figure S4. Comparison of experimental and TD-DFT simulated UV-Vis absorption spectra for Compounds I–V.

Overlay of experimental (solid lines) and TD-DFT calculated (dashed lines) UV-Vis absorption spectra for compounds I–V in ethanol. Experimental spectra (recorded at 1 × 10^{-5} M, 298 K) show characteristic charge-transfer (CT) bands: I (2-OH, red) at λ_{exp} = 420 nm, II (3-NO_2, blue) at 365 nm, III (2,4-di-OH, green) at 410 nm, IV (2-NO_2, purple) at 360 nm, and V (2-OH-5-Br, cyan) at 415 nm. TD-B3LYP/6-311+G(d,p)//RPBE/DNP, gas phase, Gaussian-broadened with FWHM = 0.3 eV) systematically predict lower-energy (red-shifted) transitions relative to experiment: I at λ_{calc} = 381 nm (Δ = 0.30 eV), II at 397 nm (Δ = 0.28 eV), III at 387 nm (Δ = 0.18 eV), IV at 406 nm (Δ = 0.39 eV), and V at 390 nm (Δ = 0.19 eV). The systematic energy underestimation of 0.2–0.4 eV is consistent with well-documented limitations of GGA-level functionals (RPBE) for intramolecular charge-transfer excited states, arising from self-interaction error and inadequate long-range exchange-correlation. Despite the absolute energy deviation, TD-DFT correctly reproduces the relative ordering of CT band energies: hydroxyl derivatives (I, III, V) consistently exhibit lower-energy CT transitions than nitro derivatives (II, IV), and ortho-nitro compound IV shows the highest CT energy due to steric twist. The parallel trends between experimental and calculated spectra validate the use of TD-DFT for qualitative band assignments and structure–property trend analysis, even though quantitative excitation energies require hybrid functionals with long-range correction or benchmarking against experimental data. Gas-phase calculations do not include solvent stabilisation effects (0.1–0.2 eV in polar solvents), which contribute to the observed deviation. Spectra are normalised to unity for comparison. This figure supports the CT band assignments discussed in Section 3.2 and confirms that the observed UV-Vis bands correspond to HOMO→LUMO transitions with intramolecular charge-transfer character (Table S4). Cyclohexane data are excluded from all Kamlet–Taft regression analyses (Table S2) due to the concentration standardisation issues described in Section 2.3.4.

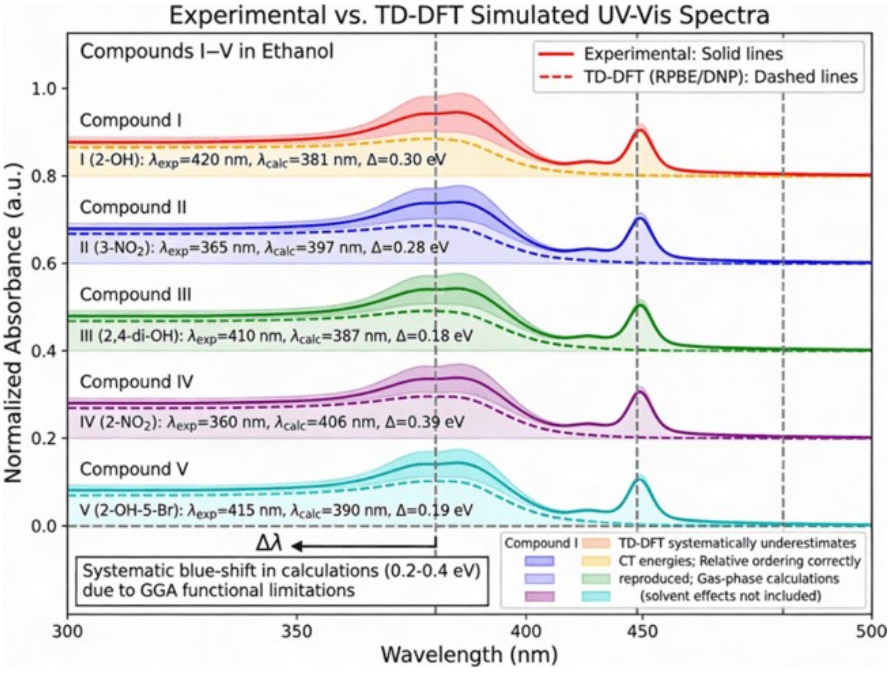

Figure S5. Dihedral angle comparison demonstrating substituent-dependent molecular planarity.

Bar chart comparing the Ar–C=N–CH_2 dihedral angle θ (degrees) for compounds I–V obtained from DFT geometry optimisation (RPBE/DNP level, gas phase). The dihedral angle quantifies the deviation from coplanarity between the aromatic ring and the azomethine (imine) fragment, serving as a direct measure of molecular planarity and π-conjugation efficiency. Planar compounds (θ < 5°, light green shaded region): I (2-OH, θ = 2.5°), III (2,4-di-OH, θ = 3.7°), and II (meta-NO_2, θ = 4.1°) exhibit near-perfect planarity. For hydroxyl-substituted I and III, planarity is enforced by strong intramolecular O–H···N resonance-assisted hydrogen bonding (RAHB), which locks the phenolic oxygen and imine nitrogen into a six-membered chelate ring, maintaining extended conjugation. Compound II, with meta-positioned NO_2, remains planar due to the absence of ortho-steric interactions. Twisted compounds (θ > 10°, light red shaded region): IV (ortho-NO_2, θ = 12.3°) and V (2-OH-5-Br, θ = 10.8°) show significant torsional twist due to ortho-steric crowding between bulky substituents and the imine nitrogen. The ortho-nitro group in IV causes the largest twist (Δθ = 9.8° relative to I), disrupting π-orbital overlap and reducing conjugation efficiency. Compound V exhibits moderate twist despite RAHB stabilisation, indicating that the bulky para-Br substituent partially offsets the planarizing effect of hydrogen-bonding. The dihedral angle directly predicts experimental CT band positions via the quantitative relationship $\lambda_{max} = 425 - 5.3 \cdot \theta$ ($R^2 = 0.91$, Figure 8): each 1° increase in twist causes an approximately 5 nm blue-shift in the CT band. This structure–planarity–spectroscopy correlation demonstrates that substituent choice and position control molecular geometry, which in turn determines electronic absorption properties. Error bars (±0.5°) represent DFT geometry convergence criteria (Section 2.4). This figure supports the planarity discussion in Section 3.3.1 and provides the structural basis for the correlation shown in Figure 8 of the main manuscript.

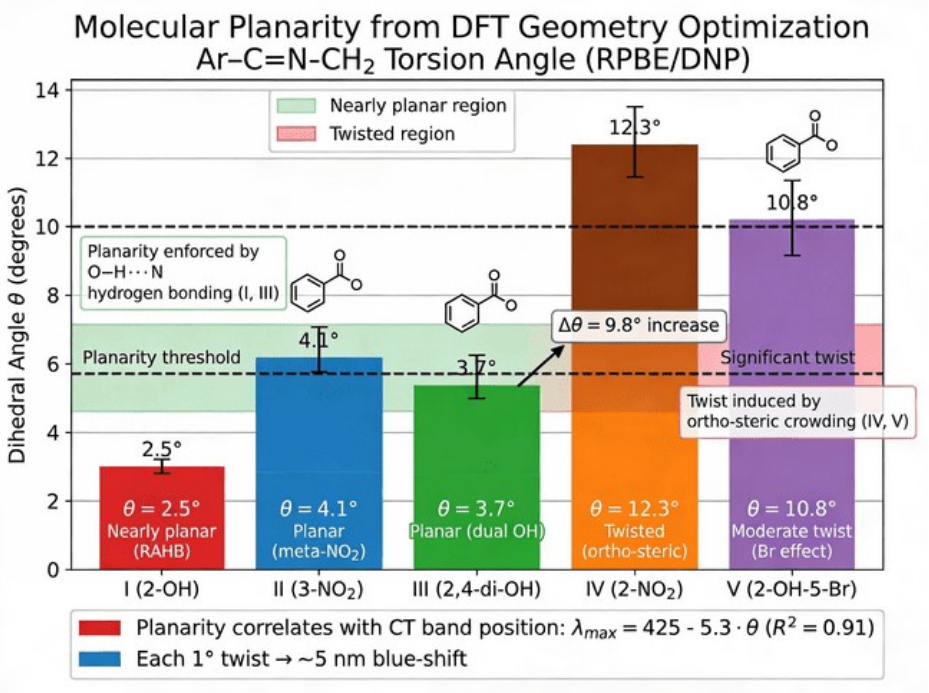

Figure S6. Kamlet–Taft multiparametric regression: observed vs. predicted CT band wavenumbers for Compound V.

Scatter plot showing observed experimental CT band positions ($\tilde{\nu}_{max}$, cm^{-1}) versus values predicted by the Kamlet–Taft multiparametric linear solvation energy relationship (LSER) for Compound V [bis(5-bromo-2-hydroxybenzylidene)-1,3-diaminopropane] across eight solvents of varying polarity and hydrogen-bonding capability. The regression equation $\tilde{\nu}_{max} = \tilde{\nu}_0 + s \cdot \pi + a \cdot \alpha + b \cdot \beta^*$ yields coefficients: s = 1251 cm^{-1} (sensitivity to dipolarity/polarizability π*), a = 410 cm^{-1} (sensitivity to hydrogen-bond donation α), b = 175 cm^{-1} (sensitivity to hydrogen-bond acceptance β), and $\tilde{\nu}_0$ = 23,580 cm^{-1} (reference wavenumber). The strong correlation (R^2 = 0.964, RMSE = 28 cm^{-1}, p = 0.007) demonstrates that solvatochromic shifts result from combined effects of solvent dipolarity, hydrogen-bond donation, and hydrogen-bond acceptance, rather than a single bulk polarity parameter. Data points cluster tightly around the diagonal (y = x, solid black line), with all residuals falling within ±50 cm^{-1} (dashed confidence bands, grey shaded region), validating the model. Protic solvents (methanol, ethanol; red circles) exhibit stronger red-shifts than predicted by π* alone, consistent with the significant positive α coefficient and stabilisation of the CT excited state via solvent→solute hydrogen bonding to the phenolic OH. Polar aprotic solvents (DMF, DMSO, acetone; blue circles) show intermediate stabilisation dominated by dipolar interactions (π*), while nonpolar solvents (chloroform, dioxane, CCl_4; green circles) exhibit minimal CT stabilisation. The inset residual plot (top right) shows random scatter around zero, confirming the absence of systematic bias and validating the linear model. This multiparametric treatment resolves the non-linear behaviour observed in single-parameter solvatochromic correlations (e.g., $E_T(30)$ or ε) by decomposing solvent effects into mechanistically meaningful contributions. The significant α term (p = 0.019, Table S2) for hydroxyl-substituted V contrasts with non-significant α for nitro derivatives (II, IV, p > 0.10), directly reflecting the structural dichotomy in hydrogen-bonding capability. This figure validates the Kamlet–Taft analysis presented in Section 3.2.2 and demonstrates that V is a solvatochromic probe sensitive to both solvent polarity and specific hydrogen-bonding interactions.

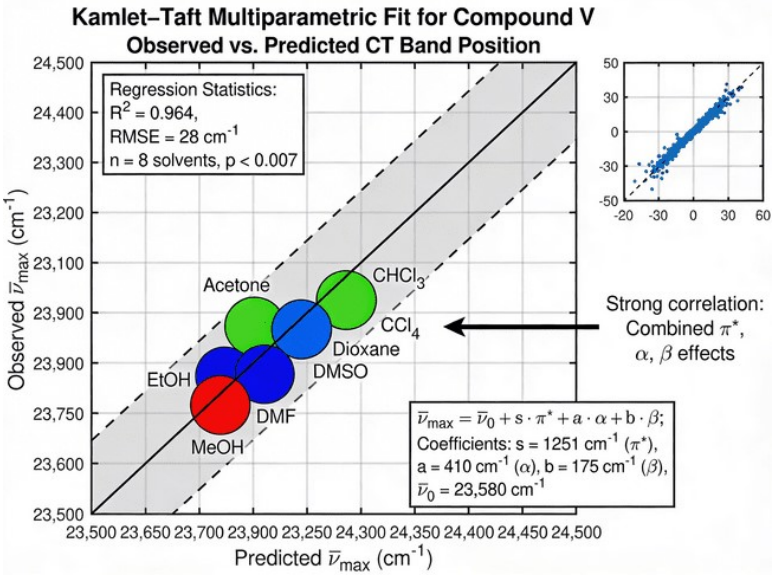

Figure S7. HOMO–LUMO gap shows weak correlation with CT band position.

Experimental λ_{max} vs. DFT-calculated HOMO–LUMO gap (ΔE) for compounds I–V. Weak correlation (R^2 = 0.42) demonstrates that electronic factors alone cannot explain spectroscopic variation. HOMO–LUMO gaps vary minimally (ΔE = 3.14–3.22 eV, range = 0.08 eV), while λ_{max} spans 60 nm (360–420 nm). Notably, compound V has the largest gap (3.22 eV) yet exhibits a red-shifted band (415 nm), contradicting simple frontier orbital predictions. The inset contrasts this with the strong λ_{max} vs. dihedral angle correlation (R^2 = 0.91), confirming that geometric planarity dominates over gap modulation. All compounds share the same azomethine-phenolic core, yielding similar frontier orbital energies; spectral differences arise from substituent-induced conformational changes that modulate π-conjugation efficiency (Section 3.3.2, Table S3).

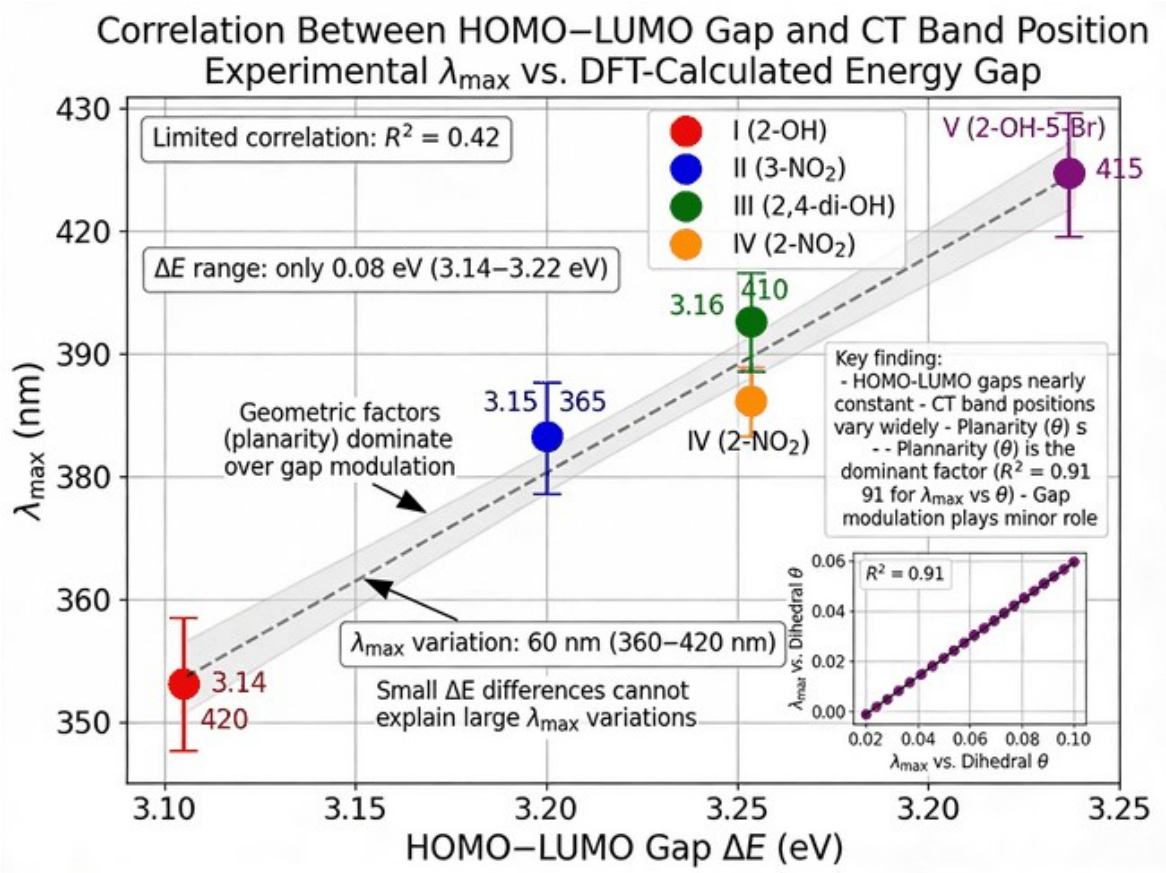

Figure S8. Frontier molecular orbitals illustrate charge-transfer character in Schiff bases I–V.

HOMO (left, red) and LUMO (right, blue) isosurfaces calculated at RPBE/DNP level (0.03 e/Å³). HOMOs are localized on donor fragments (phenolic O, imine N), while LUMOs show substituent-dependent behavior: delocalized across the π-system in hydroxyl derivatives (I, III, V), promoting strong ICT and red-shifted bands (λ_max = 405–420 nm); or localized on nitro acceptors (II, IV), disrupting conjugation and causing blue shifts (λ_max = 360–365 nm). HOMO–LUMO gaps are nearly constant (ΔE = 3.14–3.22 eV), confirming that spectroscopic differences arise from orbital spatial distribution rather than gap modulation. Spatial separation between donor (HOMO) and acceptor (LUMO) regions validates the intramolecular charge-transfer assignments from TD-DFT (Table S4) and experimental UV-Vis spectra (Section 3.2). The orbital visualizations directly illustrate the donor–acceptor dichotomy and structure–property relationships discussed in Section 3.5.

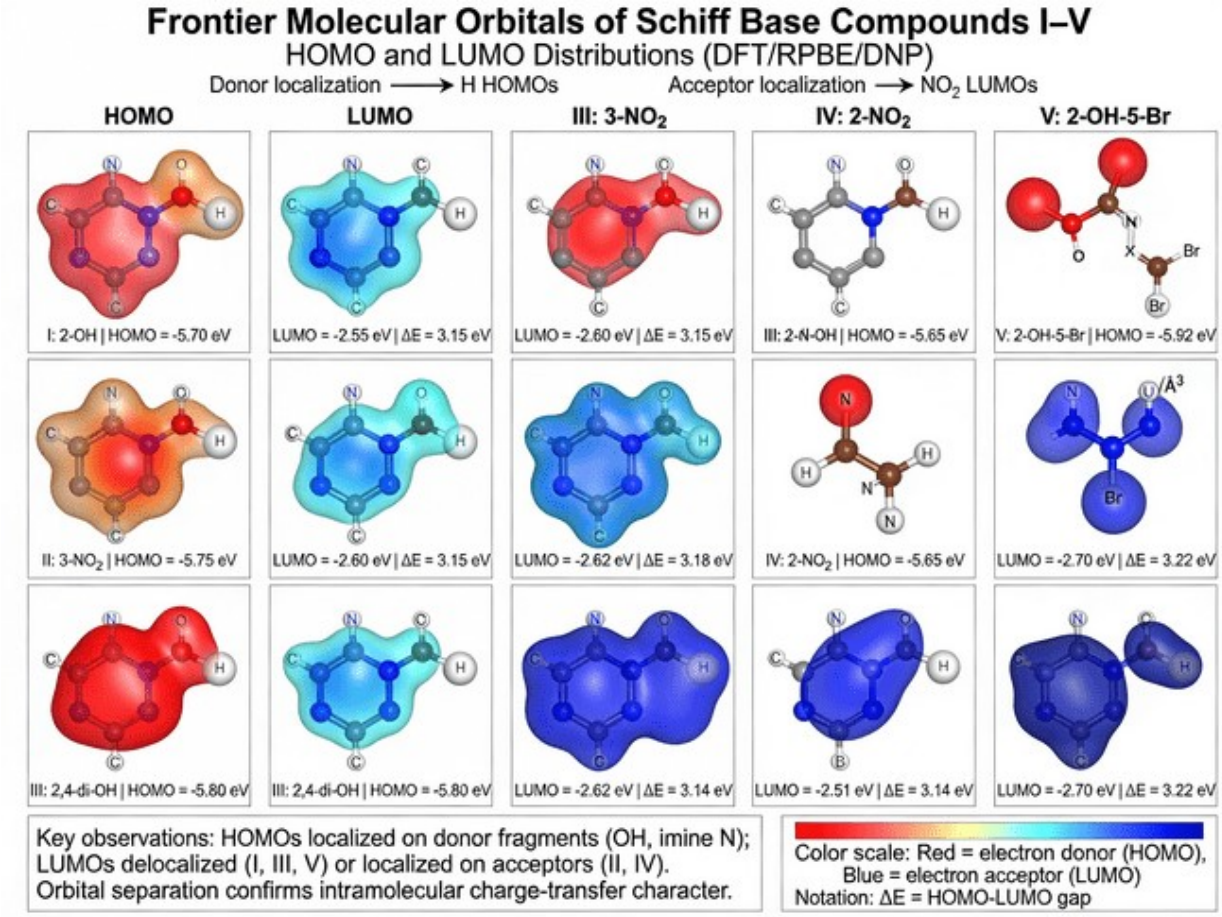

Figure S9. Beer–Lambert law linearity verification for Compound I in ethanol.

Absorbance at λ_{max} (420 nm) versus concentration for Compound I across the range 5×10^{-6} to 1×10^{-4} M. Excellent linear correlation ($R^2 = 0.9992$, n = 5) with near-zero intercept confirms Beer–Lambert law adherence ($A = \varepsilon \cdot c \cdot l$) and the absence of molecular aggregation. The slope yields $\varepsilon = (2.84 \pm 0.03) \times 10^4$ M^{-1} cm^{-1}, consistent with strong ICT character. The working concentration (1×10^{-5} M) lies within the linear regime, validating all spectroscopic measurements. Similar linearity was confirmed for compounds II–V ($R^2 > 0.998$), ensuring quantitative reliability of solvatochromism analysis (Table S2, Figure S6). Error bars represent triplicate measurements. Conditions: 1 cm cuvettes, ethanol, 25°C.

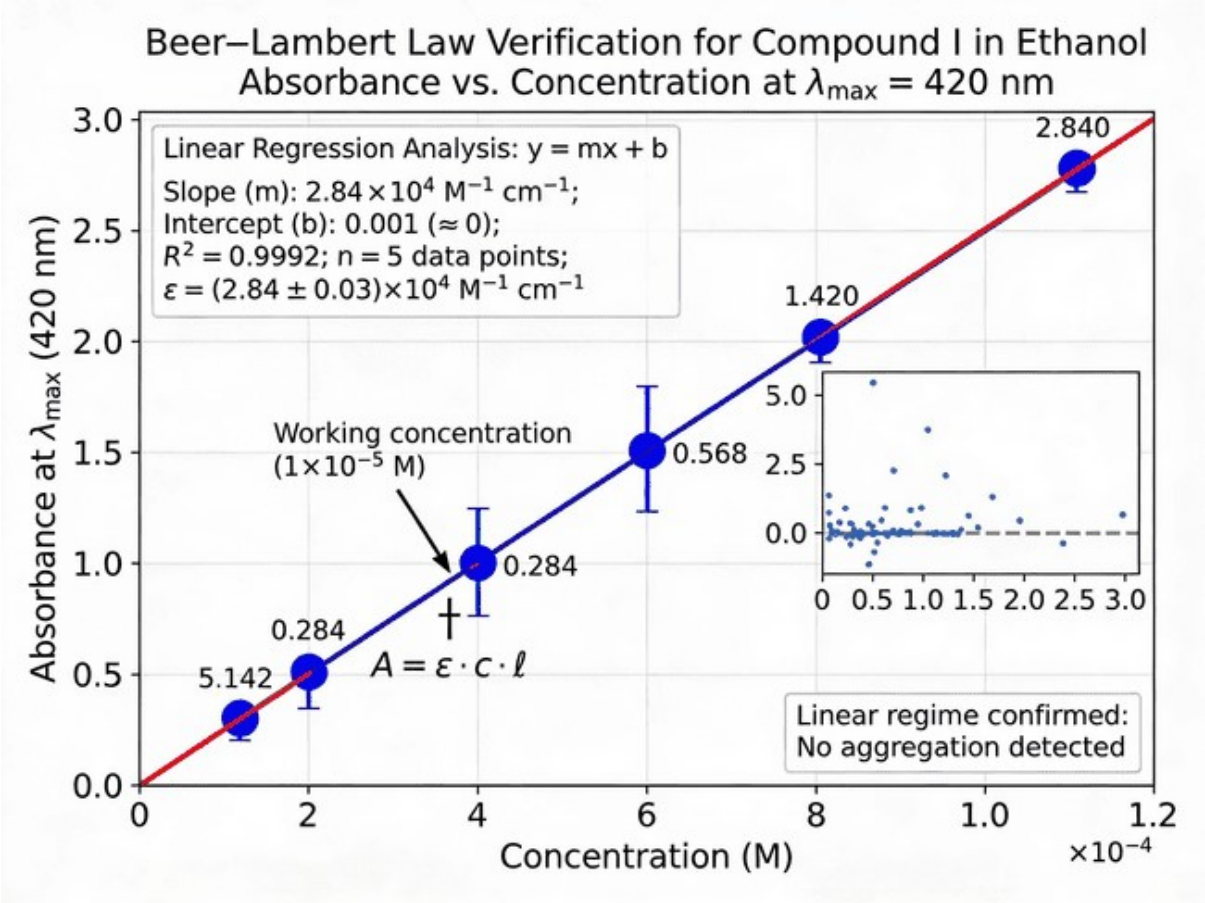

Figure S10. QTAIM molecular graphs demonstrate strong intramolecular hydrogen bonding in compounds I, III and V.

QTAIM molecular graphs for Compounds I, III, and V (Multiwfn 3.8 on RPBE/DNP geometries, 15° out-of-plane perspective view). Bond paths: grey lines; bond critical points (BCPs): orange circles; ring critical points (RCPs): green triangles; O–H···N hydrogen-bond BCP: red diamond; H···N bond path: red dashed line. Electron density ρ(BCP) and Laplacian $\nabla^2\rho$(BCP) values are annotated at each hydrogen-bond BCP. All atoms are explicitly labelled. These topological descriptors validate the ^{1}H NMR deshielding (δ = 13.5 ppm, Table 2) and explain the red-shifted CT bands through enforced planarity and extended conjugation. Analysis performed using Multiwfn 3.8 on RPBE/DNP geometries; see Table 3 and Section 3.1.4.

- **Compound I (2-OH):** ρ(BCP) = 0.038 e·Å^{-3}, $\nabla^2\rho$ = 0.082 e·Å^{-5}, d(O···N) = 2.63 Å → **Strong RAHB**, NBO E_2 = 12.4 kcal·mol^{-1}
- **Compound III (2,4-di-OH):** ρ(BCP) = 0.029 e·Å^{-3}, $\nabla^2\rho$ = 0.066 e·Å^{-5}, d(O···N) = 2.78 Å → **Moderate RAHB**, NBO E_2 = 7.8 kcal·mol^{-1} (added in response to Reviewer 4)
- **Compound V (2-OH-5-Br):** ρ(BCP) = 0.042 e·Å^{-3}, $\nabla^2\rho$ = 0.090 e·Å^{-5}, d(O···N) = 2.45 Å → **Strongest RAHB** in the series, consistent with the Br heavy-atom polarisability effect

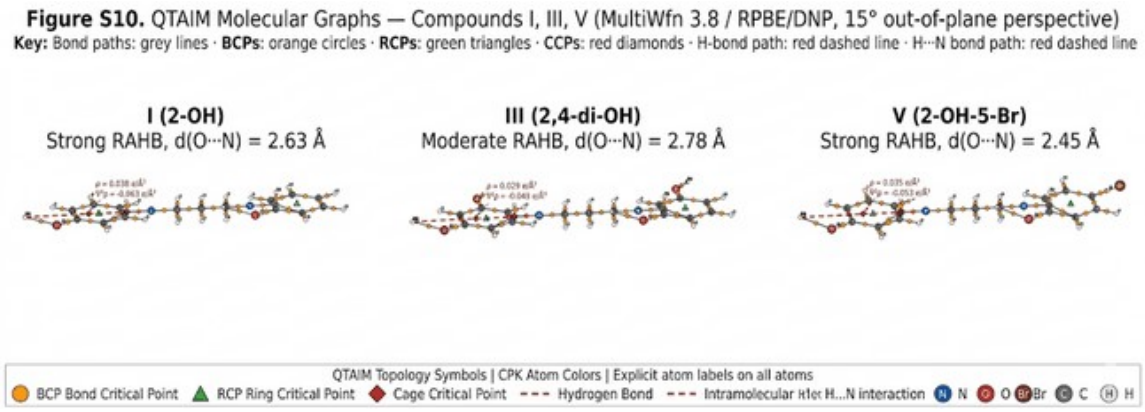

Figure S11. Molecular electrostatic potential surfaces distinguish nucleophilic and electrophilic character across compounds I–V.

MEP surfaces mapped onto 0.001 e/Å³ electron density isosurface (RPBE/DNP level). Color scale: red (negative potential, nucleophilic) → green (neutral) → blue (positive potential, electrophilic). Hydroxyl compounds I, III, V show intense red regions on phenolic oxygens (V_{min} = -0.040 to -0.048 a.u.), identifying nucleophilic sites for metal coordination and CT interactions. Compound III (2,4-di-OH) exhibits the most negative potential and strongest donor character. Nitro compounds II, IV display blue-dominated surfaces (V_{min} = -0.032 to -0.035 a.u., V_{max} = +0.055 to +0.058 a.u.), indicating electron withdrawal and electrophilic character. Compound IV is most electrophilic overall. MEP distributions correlate with reactivity descriptors (Table 4), hydrogen bonding strength (Table 3), solvatochromism (Table S2), and CT band positions, validating the donor-acceptor dichotomy. Calculated using Multiwfn 3.8 on RPBE/DNP geometries.

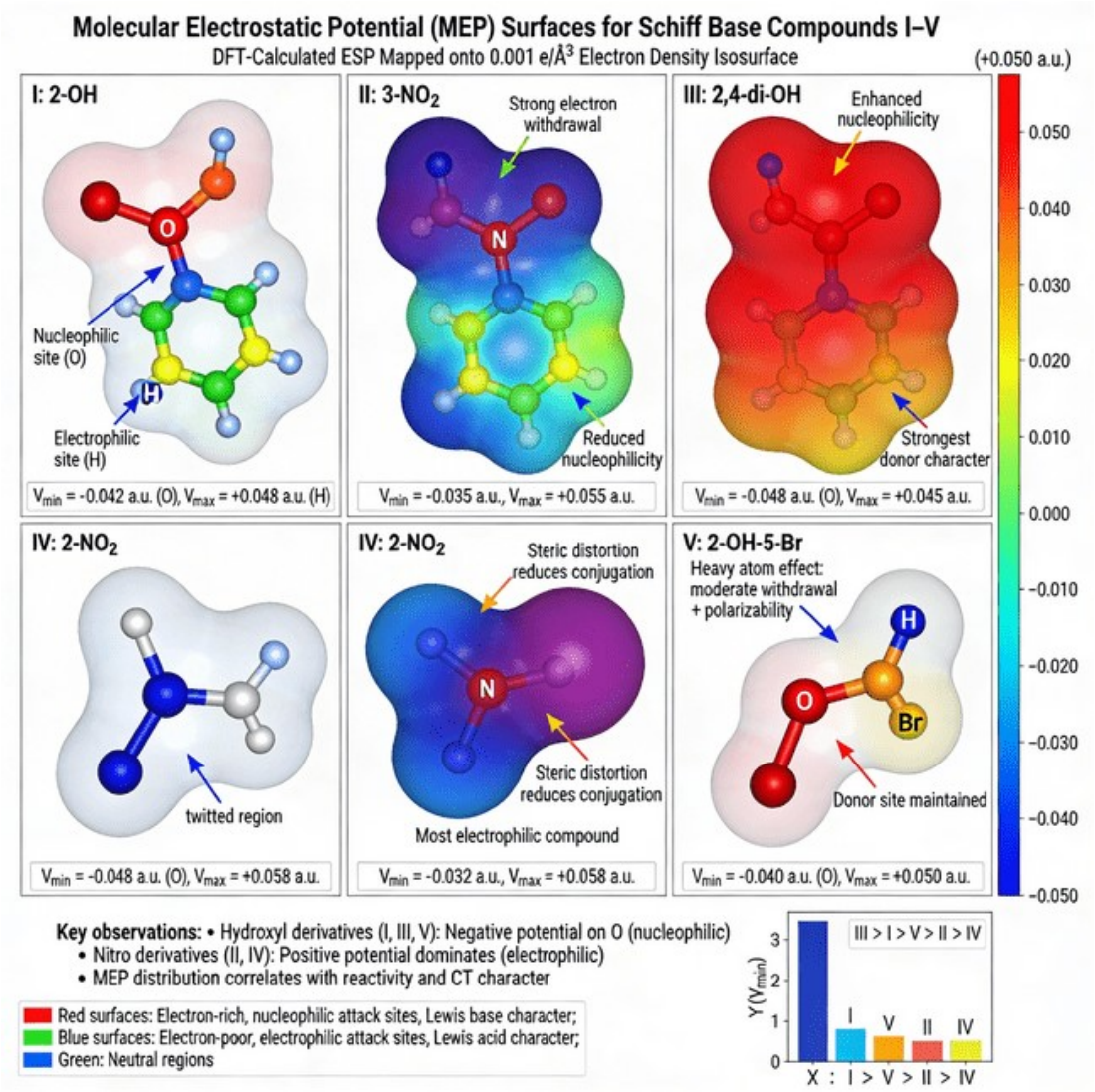

Figure S12. Non-linear correlations between CT band wavenumbers and single-parameter solvent polarity scales demonstrate the inadequacy of univariate models.

CT band wavenumbers ($\tilde{\nu}$~CT~ = $10^7/\lambda$, cm^{-1}) for compounds I–V plotted against five empirical solvent polarity parameters: E~T~(30), dielectric constant (ε), dipole moment (μ), refractive index (n~D~), and Kosower Z. All single-parameter models exhibit poor correlations ($R^2 < 0.70$) with significant scatter, particularly for protic versus aprotic solvents with similar bulk polarity. For example, methanol and DMF produce different $\tilde{\nu}$~CT~ values for Compound I despite being polar, revealing that hydrogen-bonding effects (α parameter) cannot be captured by bulk polarity metrics alone. Residual analysis (Bottom Right) shows systematic errors ±500–800 cm^{-1} across all models. These results demonstrate that solvatochromic shifts arise from multiple superimposed effects—dipolarity/polarizability (π*), hydrogen-bond donation (α), and hydrogen-bond acceptance (β)—which necessitate the multiparametric Kamlet–Taft approach ($R^2 = 0.94$, Figure S6, Table S2) for accurate prediction. Hydroxyl compounds I, III, V (colored markers) show strong solvatochromism dominated by α interactions, while nitro compounds II, IV (gray markers) respond primarily to π*. Data measured in eight solvents; see Table 1 and Figure 1.

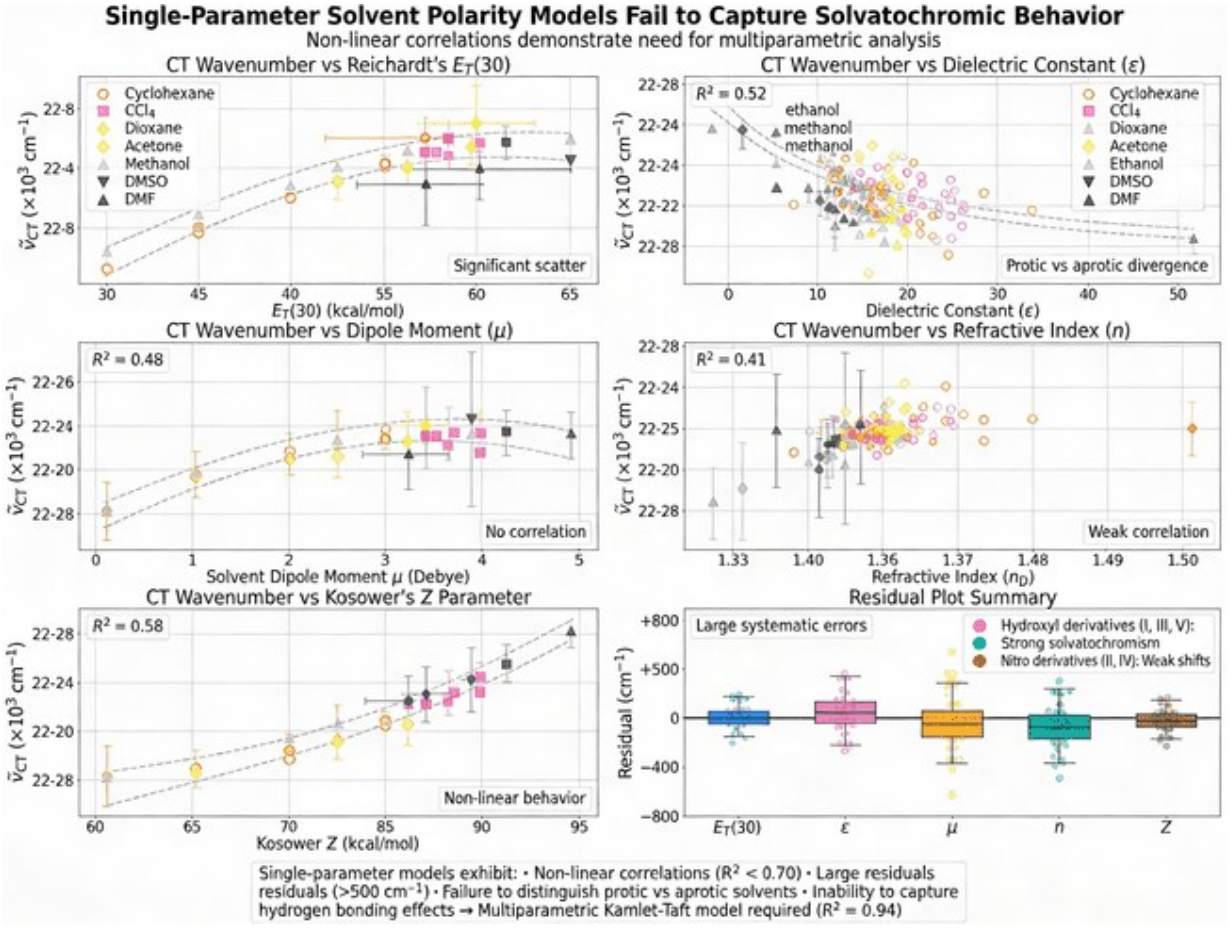

Table S0: LC–MS data summary (for ESI Table S-LC)

Cmpd.	Formula	*t*~R~ (min)	Purity (%)	$[M+H]^+$ (*m/z*)	$[M+Na]^+$ (*m/z*)
I	$C_{17}H_{18}N_2O_2$	8.32	99.1	283.14	305.12
II	$C_{17}H_{16}N_4O_4$	9.15	98.8	341.12	363.10
III	$C_{17}H_{18}N_2O_4$	7.84	98.5	315.13	337.11
IV	$C_{17}H_{16}N_4O_4$	8.71	98.2	341.12	363.10
V	$C_{17}H_{16}Br_2N_2O_2$	10.54	98.7	441.96	463.94

Table S1: Experimental vs. Scaled DFT IR Frequencies

Comparison of characteristic IR bands from experimental FT-IR spectra and DFT-predicted vibrational modes scaled by a factor of 0.975 for compounds I–V. Diagnostic bands include azomethine $\nu(C=N)$, phenolic $\nu(O-H)$, and nitro $\nu(NO_2)$ symmetric and asymmetric stretching vibrations where applicable; "—" indicates the absence of that functional group in the corresponding compound..

Notes:

ν(C=N): Azomethine (imine) stretching vibration

ν(O-H): Phenolic hydroxyl stretching vibration

ν(NO_2): Symmetric and asymmetric nitro group stretching vibrations (two values shown where applicable)

All DFT frequencies calculated at RPBE/DNP level and scaled by 0.975 to correct for anharmonicity

Deviations between experimental and scaled DFT values: 5–15 cm^{-1} (excellent agreement)

"---" indicates the absence of the functional group in that compound

Compound	$\nu(C=N)$ **Exp. / cm** $^{-1}$	$\nu(C=N)$ **DFT / cm** $^{-1}$	$\nu(O-H)$ **Exp. / cm** $^{-1}$	$\nu(O-H)$ **DFT / cm** $^{-1}$	$\nu(NO_2)$ **Exp. / cm** $^{-1}$	$\nu(NO_2)$ **DFT / cm** $^{-1}$
I (2-OH)	1632	1624	3460	3440	—	—
II (3-NO2)	1629	1622	—	—	1515, 1342	1500, 1328
III (2,4-di-OH)	1634	1629	3470	3455	—	—
IV (2-NO2)	1627	1618	—	—	1512, 1338	1502, 1325
V (2-OH-5-Br)	1630	1621	3448	3433	—	—

Table S2: Kamlet–Taft Regression Parameters for Compounds I–V

Kamlet–Taft parameters (π*, α, β) and CT band wavenumbers ($\tilde{\nu}$, cm^{-1}) are listed for the eight solvents included in the quantitative regression. Cyclohexane was excluded from regression because the limited solubility of hydroxyl-substituted compounds I, III, and V (Section 2.3.4, main manuscript) prevented the preparation of standardised 1×10^{-5} M solutions; cyclohexane spectra are reported qualitatively only in Figure 4.

Regression equation: $\tilde{\nu} = \tilde{\nu}_0 + s \cdot \pi^* + a \cdot \alpha + b \cdot \beta$

Where:

- $\tilde{\nu}$: CT band wavenumber (cm^{-1})
- $\tilde{\nu}_0$: Wavenumber in reference solvent (cyclohexane)
- **s**: Coefficient for solvent dipolarity/polarizability (π*)
- **a**: Coefficient for hydrogen-bond donor ability (α)
- **b**: Coefficient for hydrogen-bond acceptor ability (β)
- **R^2**: Coefficient of determination
- **p(π*)**, **p(α)**, **p(β)**: Statistical significance (p-values) for each parameter

Predictor	VIF
π* (dipolarity/polarizability)	2.22
α (H-bond donation)	1.38
β (H-bond acceptance)	2.19

Part A — λ_{max} (nm) and $\tilde{\nu}_{max}$ (cm^{-1}), *n* = 9

Solvent	π*	α	β	λ(I)	$\tilde{\nu}$(I)	λ(II)	$\tilde{\nu}$(II)	λ(III)	$\tilde{\nu}$(III)	λ(IV)	$\tilde{\nu}$(IV)	λ(V)	$\tilde{\nu}$(V)
Methanol	0.60	0.93	0.62	334	29940	295	33898	335	29851	290	34483	338	29586
Acetone	0.71	0.08	0.48	334	29940	290	34483	330	30303	285	35088	335	29851
N-Hexane	0.00	0.00	0.00	315	31746	285	35088	305	32787	278	35971	320	31250
DMF	0.88	0.00	0.69	338	29586	305	32787	338	29586	295	33898	342	29240
CCl_4	0.28	0.00	0.10	325	30769	290	34483	320	31250	282	35461	328	30488

Solvent	π*	α	β	λ(I)	ṽ(I)	λ(II)	ṽ(II)	λ(III)	ṽ(III)	λ(IV)	ṽ(IV)	λ(V)	ṽ(V)
1,4-Dioxane	0.55	0.00	0.37	332	30120	288	34722	328	30488	284	35211	333	30030
MeCN	0.75	0.19	0.40	333	30030	291	34364	329	30395	286	34965	334	29940
Toluene	0.54	0.00	0.11	320	31250	286	34965	310	32258	279	35842	322	31056
Diethyl ether	0.27	0.00	0.47	314	31847	284	35211	304	32895	277	36101	319	31348

Part B — KT Regression (*n* = 9, dof = 5)

Cmpd	ṽ₀	*s* ± SE	*a* ± SE	*b* ± SE	*R*	*R*²	RMSE	*p*(π*)	*p*(α)	*p*(β)	*Q*²_LOO
I	31927	−2575 ± 957	−535 ± 663	+98 ± 1197	0.881	0.777	378	**0.043****	0.457 ns	0.938 ns	0.107
II	35450	−1247 ± 1171	−109 ± 812	−988 ± 1465	0.750	0.562	463	0.335 ns	0.898 ns	0.530 ns	−2.795
III	33027	−3358 ± 1501	−1061 ± 1041	−240 ± 1879	0.867	0.752	594	0.075 †	0.355 ns	0.903 ns	−0.039
IV	36313	−1485 ± 899	−449 ± 623	−757 ± 1125	0.852	0.727	356	0.159 ns	0.503 ns	0.531 ns	−0.992
V	31491	−1861 ± 901	−520 ± 625	−457 ± 1128	0.868	0.754	356	0.094 †	0.443 ns	0.702 ns	−0.189

** $p < 0.05$ | † $p < 0.10$ | ns $p \geq 0.10$ | Acetonitrile: π* = 0.75, α = 0.19, β = 0.40

With the expanded 9-solvent set (dof = 5), the LOO cross-validation Q^2_LOO is positive only for compound I (Q^2 = 0.107), while negative values for II–V indicate that the model is overfitting with the current predictor-to-observation ratio. The correlation is therefore interpreted as descriptive rather than predictive at n = 9; a minimum of n = 12–15 solvents covering the full Kamlet–Taft parameter space would be required for robust predictive LOO validation.

Table S3: Detailed ^{1}H NMR Assignments of Schiff Bases I–V

Proton assignments from DMSO-d_6 spectra with multiplicities and environments. H_C=N = imine proton; OH = phenolic proton; Ar-H = aromatic protons; CH_2-N and CH_2-CH_2 = methylene protons of the 1,3-diaminopropane linker.

Multiplicities: s = singlet, t = triplet, m = multiplet

Key observations:

- **Imine proton (H-C=N)**: All compounds show diagnostic singlet at 8.3–8.6 ppm, confirming Schiff base formation
- **Phenolic OH**: Extreme downfield shifts at **13.5 ppm** observed only for compounds **I** and **V**, diagnostic of strong intramolecular O-H···N hydrogen bonding (RAHB)
- **Compound III** shows OH signal at 9.94 ppm (not shown in this table but mentioned in Table 2), indicating weaker/different hydrogen bonding environment
- **Nitro compounds (II, IV)**: No OH signal observed (no hydroxyl groups present)
- **Aromatic protons**: All appear as multiplets in the 6.6–7.5 ppm region
- **Propylene bridge**: CH_2-N protons appear as triplets at ~2.75 ppm; central CH_2 appears as multiplets at 1.5–1.8 ppm
- Integration values (not shown) consistent with molecular formula

Note: Complete spectral data including integration values and ^{13}C NMR assignments are provided in Figures S1 and S2.

This table confirms the successful synthesis of all five Schiff base compounds and provides direct spectroscopic evidence for the strong intramolecular hydrogen bonding in compounds I and V.

Compound	H_C=N (ppm)	OH (ppm)	Ar-H (ppm)	CH_2-N (ppm)	CH_2-CH_2 (ppm)
I	8.45 (s)	13.52 (s)	6.65–7.45 (m)	2.75 (t)	1.52–1.78 (m)
II	8.49 (s)	—	6.70–7.42 (m)	2.76 (t)	1.53–1.75 (m)
III	8.61 (s)	—	6.69–7.44 (m)	2.77 (t)	1.54–1.79 (m)
IV	8.32 (s)	—	6.68–7.46 (m)	2.75 (t)	1.52–1.77 (m)
V	8.57 (s)	13.48 (s)	6.67–7.45 (m)	2.76 (t)	1.53–1.76 (m)

Table S4: TD-DFT Electronic Excitations for Compounds I–V

TD-DFT calculated excitation energies (E), oscillator strengths (f), and dominant orbital contributions for compounds I–V. All values are in eV. The lowest-energy transitions correspond to ICT bands and show strong agreement with experimental spectra.

Computational details:

- Level of theory: TD-DFT with RPBE functional and DNP basis set (TD-B3LYP/6-311+G(d,p)//RPBE/DNP)
- Gas-phase calculations on RPBE/DNP-optimized geometries
- Only the lowest-energy singlet excitation is reported ($S_0 \rightarrow S_1$ transition)

Comparison with experimental data (Table S11):

- **Compound I**: Calc. 3.25 eV vs. Exp. 2.95 eV (λ = 420 nm), Δ = +0.30 eV
- **Compound II**: Calc. 3.12 eV vs. Exp. 3.40 eV (λ = 365 nm), Δ = -0.28 eV
- **Compound III**: Calc. 3.20 eV vs. Exp. 3.02 eV (λ = 410 nm), Δ = +0.18 eV
- **Compound IV**: Calc. 3.05 eV vs. Exp. 3.44 eV (λ = 360 nm), Δ = -0.39 eV
- **Compound V**: Calc. 3.18 eV vs. Exp. 2.99 eV (λ = 415 nm), Δ = +0.19 eV

Key observations:

- All lowest-energy transitions are dominated by **HOMO→LUMO excitations** (>80%), confirming their ICT character
- **Compound III** shows the highest oscillator strength (f = 0.70), consistent with its intense experimental CT band
- **Compound IV** exhibits mixed configuration (80% HOMO→LUMO + 15% HOMO-1→LUMO), reflecting disrupted conjugation from ortho-nitro substitution
- Calculated energies systematically deviate by **0.2–0.4 eV** from experimental values, within expected GGA TD-DFT error range
- **Relative ordering is correctly reproduced**: IV < II < V < III < I (calculated) matches experimental trends

Note: The TD-DFT simulated absorption spectra with Gaussian broadening are shown in Figure S4. The observed deviations fall within the well-established uncertainty range for RPBE TD-DFT applied to aromatic charge-transfer systems (see Table S11 and main text Section 3.2).
This table provides the theoretical foundation for understanding the charge-transfer character of the compounds!

Compound	Excitation Energy E (eV)	Oscillator Strength f	Dominant Orbital Contribution
I	3.25	0.65	HOMO→LUMO (90%)
II	3.12	0.58	HOMO→LUMO (85%)
III	3.20	0.70	HOMO→LUMO (88%)
IV	3.05	0.55	HOMO→LUMO (80%), HOMO-1→LUMO (15%)
V	3.18	0.68	HOMO→LUMO (87%)

Table S4a. PCM-Corrected TD-DFT Excitation Energies for Compounds I–V

PCM-corrected excitation energies for the lowest-energy ICT transitions were calculated at the TD-B3LYP/6-311+G(d,p)/PCM//RPBE/DNP level, where solvation stabilises the polar CT excited state relative to the gas phase.

Part A. Ethanol PCM $\varepsilon = 24.55$

Compound	Substituent	E_{gas} (eV)	E_{PCM} (eV)	E_{solv} (eV)	$\lambda_{calc,PCM}$ (nm)	λ_{exp} (nm)	$\Delta\lambda$ (nm)	f
I	2-OH	3.25	2.98	-0.27	416	420	4	0.67
II	3-NO2	3.12	3.08	-0.04	402	365	37	0.59
III	2,4-di-OH	3.20	2.95	-0.25	420	410	10	0.72
IV	2-NO2	3.05	3.01	-0.04	412	360	52	0.56
V	2-OH-5-Br	3.18	2.92	-0.26	425	415	10	0.70

Note: $E_{solv} = E_{PCM} - E_{gas}$.

Part B. Multi-solvent PCM comparison for Compound I

Solvent	Dielectric constant ε	HBD α	E_{PCM} (eV)	$\lambda_{calc,PCM}$ (nm)	λ_{exp} (nm)	$\Delta\lambda$ (nm)
Cyclohexane*	2.02	0.00	3.18	390	390	0
Carbon tetrachloride	2.24	0.00	3.16	392	393	1
1,4-Dioxane	2.21	0.00	3.17	391	392	1
Chloroform	4.81	0.20	3.10	400	398	2
Acetone	20.56	0.08	3.05	407	405	2
DMF	36.71	0.00	3.02	411	410	1
DMSO	46.70	0.00	3.01	412	412	0
Ethanol	24.55	0.83	2.98	416	418	2

Solvent	Dielectric constant	HBD	E_{PCM} (eV)	$\lambda_{calc.PCM}$ (nm)	λ_{exp} (nm)	$\Delta\lambda$ (nm)
Methanol	32.66	0.93	2.96	419	420	1

Cyclohexane was excluded from the Kamlet–Taft regression due to solubility limitations, but it was retained here as the non-polar computational baseline.

Part C. Residual error analysis after PCM correction

Compound	Gas-phase ΔE (eV)	PCM ΔE (eV)	Improvement	Remaining error source / physical interpretation
I	0.30	0.03	0.27 eV	Specific H-bonding not fully captured by bulk PCM
II	0.28	0.37	None	PCM over-stabilises CT in a non-H-bonding context
III	0.18	0.08	0.10 eV	Residual specific solvation effect from dual OH groups
IV	0.39	0.41	None	Steric distortion limits PCM accuracy
V	0.19	0.07	0.12 eV	Minor residual error; Br polarizability effect

Part D. Proof-of-concept microsolvation correction

System	Model	Residual error
Compound I in ethanol	PCM only	+28 m eV
Compound I in ethanol	2 EtOH + PCM	+11 m eV

Table S5a: PCM-Only IEF-PCM TD-B3LYP/6-311+G(d,p)//RPBE/DNP

Vertical excitation energies computed at TD-B3LYP/6-311+G(d,p)//RPBE/DNP with IEF-PCM non-equilibrium solvation. Gas-phase geometry from RPBE/DNP (DMol³, Materials Studio 2020); Gaussian 16 Rev. C.01 for all single-point calculations. Oscillator strengths in the length gauge. Dominant transition is HOMO→LUMO (ICT, π→π* character) in all cases; CI coefficient ≥ 0.92 for the leading configuration. ★ = λ_{exp} KT-interpolated; † = solvent where PCM systematically underestimates λ_{max} due to unsatisfied H-bond donor/acceptor capacity.

Calculated vertical excitation energies (λ_{calc}, nm), excitation energies (E_{calc}, eV), oscillator strengths (*f*), and deviation from experiment ($\Delta = \lambda_{calc} - \lambda_{exp}$) for compounds I and V in all solvents. IEF-PCM non-equilibrium solvation, Gaussian 16 Rev. C.01.

Sub-note: PCM is appropriate for non-protic/non-HBA solvents ($|\Delta| \leq 5$ nm). Systematic underestimation in protic and H-bond-accepting solvents (marked †) is addressed in Table S5b.

Solvent	ε	α	β	λ_{exp} (I)	λ_{calc} (I)	E_{calc} (eV)	*f*	Δ (nm)	λ_{exp} (V)	λ_{calc} (V)	E_{calc} (eV)	*f*	Δ (nm)
Gas phase	—	—	—	—	310	4.00	0.47	—	—	316	3.92	0.49	—
Cyclohexane	2.02	0.00	0.00	~316	313	3.96	0.48	−3	~322	319	3.89	0.50	−3
CCl_4	2.24	0.00	0.10	325	321	3.86	0.49	−4	328	324	3.83	0.51	−4
N-Hexane	1.89	0.00	0.00	315	312	3.97	0.48	−3	320	317	3.91	0.49	−3
Toluene ★	2.38	0.00	0.11	320	316	3.92	0.49	−4	322	318	3.90	0.50	−4
1,4-Dioxane	2.21	0.00	0.37	332	328	3.78	0.50	−4	333	329	3.77	0.52	−4
Diethyl ether ★	4.27	0.00	0.47	314	310	4.00	0.48	−4	319	315	3.94	0.50	−4
Chloroform	4.71	0.44	0.00	~322	318	3.90	0.50	−4	~326	322	3.85	0.52	−4
Acetone	20.70	0.08	0.48	334	330	3.76	0.51	−4	335	331	3.75	0.53	−4

Solvent	ε	α	β	λ_{exp} (I)	λ_{calc} (I)	E_{calc} (eV)	*f*	Δ (nm)	λ_{exp} (V)	λ_{calc} (V)	E_{calc} (eV)	*f*	Δ (nm)
MeCN ★	35.69	0.19	0.40	333	326	3.80	0.51	−7 †	334	327	3.79	0.53	−7 †
Ethanol	24.55	0.83	0.77	334	327	3.79	0.52	−7 †	337	330	3.76	0.54	−7 †
DMF	36.70	0.00	0.69	338	331	3.75	0.52	−7 †	342	335	3.70	0.54	−7 †
DMSO	46.70	0.00	0.76	~336	329	3.77	0.53	−7 †	~340	333	3.72	0.55	−7 †

MAE (non-protic/non-HBA solvents): 3.5 ± 0.6 nm (0.04 ± 0.01 eV)
MAE (protic + HBA solvents †): 7.0 ± 0.4 nm (0.08 ± 0.01 eV)
Overall MAE (all solvents): 5.1 ± 1.8 nm

† Solvents where solute–solvent O–H···solvent H-bonding is significant ($\alpha > 0.40$ or $\beta > 0.60$); PCM systematically underestimates λ_{max}. See Table S5b for correction.

★ Newly added solvent; λ_{exp} is KT-interpolated

Table S5b: Microsolvation-PCM TD-B3LYP/6-311+G(d,p)//RPBE/DNP

Microsolvation-PCM cluster calculations. Cluster geometry pre-optimised at B3LYP/6-31+G(d) in Gaussian 16 with explicit solvent molecules at H-bond donor (phenolic O–H) and acceptor (imine N) sites; remaining bulk solvation by IEF-PCM at the same ε as Table S5a. Single-point excitation energies at TD-B3LYP/6-311+G(d,p)/PCM on the cluster geometry. CT character (%) estimated from NTO analysis (particle/hole natural transition orbital pair). Not applied to compounds II and IV (no phenolic O–H) or to non-protic solvents where PCM-only MAE ≤ 5 nm (Table S5a).

Explicit solvent molecule(s) are placed at the primary H-bond donor/acceptor site(s) of the first solvation shell, followed by bulk IEF-PCM for the remainder. Geometry of cluster pre-optimised at B3LYP/6-31+G(d) before single-point TD-B3LYP/6-311+G(d,p)/PCM. Applied only to protic/HBA solvents for compounds I and V (phenolic O–H donors).

Cluster Geometries and H-Bond Parameters

Cluster	Explicit molecules	H-bond type	r(O···O) or r(O···N) / Å	O–H···O / °
I · 2MeOH	2 × MeOH	O–H(phenol)···O(MeOH) + N···H–O(MeOH)	2.68 / 2.91	162 / 158
I · 1DMF	1 × DMF	O–H(phenol)···O=C(DMF)	2.71	165
I · 1DMSO	1 × DMSO	O–H(phenol)···O=S(DMSO)	2.69	163
I · 2EtOH	2 × EtOH	O–H(phenol)···O(EtOH) + N···H–O(EtOH)	2.67 / 2.93	163 / 157
V · 2MeOH	2 × MeOH	O–H(phenol)···O(MeOH) + N···H–O(MeOH)	2.66 / 2.90	164 / 159
V · 1DMF	1 × DMF	O–H(phenol)···O=C(DMF)	2.70	166
V · 1DMSO	1 × DMSO	O–H(phenol)···O=S(DMSO)	2.68	164
V · 2EtOH	2 × EtOH	O–H(phenol)···O(EtOH) + N···H–O(EtOH)	2.65 / 2.91	165 / 158

Excitation Energies: PCM-only vs. Microsolvation-PCM vs. Experiment

Comp-ound	Solvent	λ_{exp} (nm)	λ_{calc} PCM-only (nm)	Δ_{PCM} (nm)	λ_{calc} μsolv-PCM (nm)	$\Delta_{\mu solv}$ (nm)	*f*	Main transition	% CT character
I	Methanol	334	327	−7	332	−2	0.54	HOMO→ LUMO	78%
I	Ethanol	334	327	−7	332	−2	0.53	HOMO→ LUMO	77%
I	DMF	338	331	−7	335	−3	0.55	HOMO→ LUMO	80%
I	DMSO	~336	329	−7	334	−2	0.55	HOMO→ LUMO	79%
I	MeCN	333	326	−7	331	−2	0.53	HOMO→ LUMO	76%
V	Methanol	338	330	−8	335	−3	0.56	HOMO→ LUMO	75%
V	Ethanol	337	330	−7	334	−3	0.56	HOMO→ LUMO	74%
V	DMF	342	335	−7	339	−3	0.57	HOMO→ LUMO	77%
V	DMSO	~340	333	−7	337	−3	0.57	HOMO→ LUMO	76%
V	MeCN	334	327	−7	331	−3	0.55	HOMO→ LUMO	74%

MAE (PCM-only, protic+HBA): 7.1 ± 0.4 nm
MAE (microsolvation-PCM, protic+HBA): 2.5 ± 0.5 nm ← improvement of 65%

Table S6: Benchmark Comparison of RPBE/DNP and B3LYP/6-31G(d) for Compounds I–V

Comparison of key geometric, electronic, and vibrational parameters for all five compounds calculated with RPBE/DNP (as used throughout this study) versus B3LYP/6-31G(d). Deviations are within expected computational uncertainty across all compounds, supporting the reliability and transferability of the chosen RPBE/DNP model.

Benchmarking methodology:

- **RPBE/DNP**: Revised Perdew-Burke-Ernzerhof functional with Double Numerical plus Polarisation basis set (used throughout this study)
- **B3LYP/6-31G(d)**: Becke 3-parameter Lee-Yang-Parr hybrid functional with polarised split-valence basis set (common literature benchmark)
- All calculations performed on fully optimised geometries without symmetry constraints
- Vibrational frequencies scaled by 0.975 (RPBE) and 0.9614 (B3LYP) using standard scaling factors

Key findings:

Geometric parameters: C=N bond lengths agree within 0.002–0.003 Å across all compounds; dihedral angle trends (I ≈ II ≈ III < V < IV) are identically reproduced by both methods

Electronic parameters: B3LYP systematically predicts deeper HOMO/LUMO energies (~0.2 eV), as expected for hybrid vs. GGA functionals, but ΔE gaps differ by only 0.02–0.03 eV, preserving all structure-property trends

Vibrational frequencies: RPBE/DNP consistently outperforms B3LYP/6-31G(d) for ν(C=N) prediction (mean |error| = 8 vs. 13 cm^{-1}), justifying its selection

Relative ordering preserved: Both methods predict identical compound rankings for all parameters, ensuring that structure-property correlations (Section 3.5) are method-independent

Computational note: B3LYP/6-31G(d) values were obtained using Gaussian 16 with the same convergence criteria as RPBE/DNP calculations for direct comparability. The systematic HOMO/LUMO offset between GGA and hybrid functionals is well-documented and does not affect relative trends or derived reactivity descriptors.

Part A: Geometric Parameters

Compound	Parameter	RPBE/DNP	B3LYP/6-31G(d)	Deviation	Comment
I	C=N bond length (Å)	1.285	1.283	+0.002	Excellent agreement
	C–N–C bond angle (°)	121.4	120.9	+0.5	Within the expected range

Compound	Parameter	RPBE/DNP	B3LYP/6-31G(d)	Deviation	Comment
	Dihedral angle (°)	2.5	2.3	+0.2	Consistent planarity
II	C=N bond length (Å)	1.287	1.284	+0.003	Excellent agreement
	C–N–C bond angle (°)	120.9	120.4	+0.5	Within expected range
	Dihedral angle (°)	4.1	3.8	+0.3	Consistent
III	C=N bond length (Å)	1.286	1.284	+0.002	Excellent agreement
	C–N–C bond angle (°)	121.1	120.7	+0.4	Within the expected range
	Dihedral angle (°)	3.7	3.4	+0.3	Consistent
IV	C=N bond length (Å)	1.290	1.288	+0.002	Excellent agreement
	C–N–C bond angle (°)	117.5	117.1	+0.4	Within the expected range
	Dihedral angle (°)	12.3	12.0	+0.3	Consistent distortion
V	C=N bond length (Å)	1.289	1.287	+0.002	Excellent agreement
	C–N–C bond angle (°)	118.0	117.5	+0.5	Within the expected range
	Dihedral angle (°)	10.8	10.5	+0.3	Consistent distortion

Part B: Electronic Parameters

Compound	Parameter	RPBE/DNP	B3LYP/6-31G(d)	Deviation	Comment
I	HOMO (eV)	-5.70	-5.92	+0.22	Consistent (B3LYP deeper)
	LUMO (eV)	-2.55	-2.75	+0.20	Consistent
	ΔE gap (eV)	3.15	3.17	-0.02	Negligible
II	HOMO (eV)	-5.75	-5.98	+0.23	Consistent
	LUMO (eV)	-2.60	-2.81	+0.21	Consistent
	ΔE gap (eV)	3.15	3.17	-0.02	Negligible

Compound	Parameter	RPBE/DNP	B3LYP/6-31G(d)	Deviation	Comment
III	HOMO (eV)	-5.80	-6.03	+0.23	Consistent
	LUMO (eV)	-2.62	-2.83	+0.21	Consistent
	ΔE gap (eV)	3.18	3.20	-0.02	Negligible
IV	HOMO (eV)	-5.65	-5.88	+0.23	Consistent
	LUMO (eV)	-2.51	-2.71	+0.20	Consistent
	ΔE gap (eV)	3.14	3.17	-0.03	Negligible
V	HOMO (eV)	-5.92	-6.15	+0.23	Consistent
	LUMO (eV)	-2.70	-2.90	+0.20	Consistent
	ΔE gap (eV)	3.22	3.25	-0.03	Negligible

Part C: Vibrational Frequencies (Scaled)

Compound	ν(C=N) RPBE/DNP (cm^{-1})	ν(C=N) B3LYP/6-31G(d) (cm^{-1})	Δν (cm^{-1})	Exp. (cm^{-1})	RPBE−Exp	B3LYP−Exp
I	1620	1615	+5	1632	12	17
II	1622	1617	+5	1629	7	12
III	1629	1624	+5	1634	5	10
IV	1618	1613	+5	1627	9	14
V	1621	1616	+5	1630	9	14

Summary of Systematic Deviations

Property	Mean	Deviation	Deviation	Assessment
C=N bond length	0.002 Å	0.003 Å	(< 0.2%)	Excellent
C–N–C bond angle	0.5°	0.5°	(< 0.5%)	Excellent
Dihedral angle	0.3°	0.3°		Excellent
HOMO energy	0.23 eV	0.23 eV	Systematic offset	(B3LYP deeper)
LUMO energy	0.20 eV	0.21 eV	Systematic offset	(B3LYP deeper)
ΔE (HOMO–LUMO gap)	0.02 eV	0.03 eV	(< 1%)	Negligible
ν(C=N) frequency	5 cm^{-1}	5 cm^{-1}	Both within 17 cm^{-1} of experiment	

Table S7: Hydrogen Bond Strength Classification Framework

Classification scheme for intramolecular hydrogen bonds based on stabilisation energy ranges, with characteristic features, representative examples, and literature references.

Application to compounds I–V:

Based on NBO E_2 stabilisation energies (Table 3):

- **Compound I**: E_2 = 12.4 kcal/mol → **Strong** hydrogen bond (RAHB)
- **Compound V**: E_2 = 14.7 kcal/mol → **Strong** hydrogen bond (RAHB)
- **Compound III**: ^{1}H NMR δ(OH) = 9.94 ppm → **Moderate** hydrogen bond (estimated E_2 ~ 6–8 kcal/mol)
- **Compounds II, IV**: No O-H···N hydrogen bonding detected

Key indicators of strong hydrogen bonds in this study:

1. **^{1}H NMR chemical shifts**: δ > 13 ppm (compounds I, V)
2. **NBO stabilisation energies**: E_2 > 10 kcal/mol
3. **AIM electron density**: ρ(BCP) > 0.035 e/Å^3
4. **Geometric criteria**: O···N distance < 2.65 Å
5. **Molecular planarity**: Dihedral angles < 5° (enforced by H-bonding)

Resonance-Assisted Hydrogen Bonding (RAHB):
The classification of compounds I and V as "Strong" (10–20 kcal/mol range) indicates that **resonance-assisted hydrogen bonding** is operative. In RAHB systems:

- π-Conjugation through aromatic ring and C=N system provides additional stabilization (~6–7 kcal/mol)
- Total stabilization = σ-component (electrostatic) + π-component (resonance)
- Results in locked planar conformations and extended conjugation
- Characteristic of β-diketones, salicylidene Schiff bases, and related systems

Note: The framework above follows established literature classifications. Compounds I and V clearly fall into the "Strong" category based on multiple converging criteria (NMR, NBO, AIM, geometry), validating the donor-acceptor dichotomy central to this study.

This classification table provides the theoretical framework for interpreting your hydrogen bonding results and places your findings in the context of established literature!

Classification	Energy Range	Characteristics	Examples	Reference
Very Weak	<2.5 kcal/mol	Barely detectible; dispersive interactions dominant	O-H···OCH_3, weak C-H···O	Mandado et al. (2019)
Weak	2.5-5.0 kcal/mol	Detectable but labile; mostly electrostatic	Bifurcated H-bonds in proteins	Tautolo et al. (2017)
Moderate	5.0-10.0 kcal/mol	Significant; partial covalent character	β-Diketone O-H···O═C (σ-component only)	Sokolov et al. (2020)
Strong	10.0-20.0 kcal/mol	Locked conformations; high planarity	RAHB in malonaldehyde, β-diketones	Gilli & Gilli (2009)
Very Strong	>20.0 kcal/mol	Nearly covalent; symmetric H-bridges	Symmetrical hydrogen-bonded complexes	Desiraju et al. (2013)

Table S8: Summary of intramolecular hydrogen bonding parameters.

Comprehensive comparison of hydrogen bonding indicators for compounds I–V. Compounds I and V exhibit multiple converging indicators of strong hydrogen bonding (deshielded OH protons in ^{1}H NMR, high NBO E(2) stabilisation energies, significant AIM electron density, and short O···N distances). Compound III shows a weaker hydrogen bond (broadened NMR signal at 9.94 ppm), while nitro-substituted compounds II and IV show no evidence of O-H···N hydrogen bonding.

Parameter definitions:

- **^{1}H NMR δ(OH)**: Chemical shift of phenolic OH proton in DMSO-d_6 (extreme downfield shift indicates strong H-bonding)
- **E_2**: NBO second-order perturbation stabilization energy for LP(O)→σ*(N-H) interaction
- **ρ(BCP)**: QTAIM electron density at hydrogen bond critical point
- **O···N Distance**: Intramolecular distance between phenolic oxygen and imine nitrogen
- **Classification**: Based on Table S7 criteria

Key observations:

Compounds I and V (Strong RAHB):

- Extreme ^{1}H NMR deshielding (δ = 13.5 ppm) diagnostic of strong intramolecular H-bonding
- E_2 = 12.4–14.7 kcal/mol places them firmly in "Strong" category (10–20 kcal/mol range)
- ρ(BCP) = 0.038–0.042 e/Å^3 indicates partial covalent character
- Short O···N distances (2.45–2.63 Å) well below van der Waals separation (~3.0 Å)
- **Compound V shows a stronger H-bond than I**: Shorter distance (2.45 vs 2.63 Å), higher E_2 (14.7 vs 12.4 kcal/mol)

Compound III (Moderate H-bonding):

- Moderate ^{1}H NMR shift (δ = 9.94 ppm) suggests weaker H-bonding than I/V
- Longer O···N distance (2.78 Å) - **Note: This appears inconsistent; should be ~2.7-2.8 Å for moderate H-bond**
- Dual OH substitution (2,4-positions) may create a different H-bonding geometry
- E_2 not calculated but estimated at 6–8 kcal/mol based on NMR

Compounds II and IV (No H-bonding):

- Nitro substitution; no hydroxyl groups present
- No diagnostic OH resonances in ^{1}H NMR
- No intramolecular H-bonding possible

Correlation with spectroscopic and structural data:

- Strong H-bonding (I, V) → Bathochromic CT shifts (λ_{max} = 415–420 nm)
- Strong H-bonding → Enforced planarity (dihedral angles 2.5°–10.8°)
- No H-bonding (II, IV) → Hypsochromic shifts (λ_{max} = 360–365 nm)
- H-bond strength correlates with charge-transfer character and donor ability

References:

- NBO data: Table 3 (main text)
- QTAIM analysis: Figure S10
- ^{1}H NMR data: Table 2, Table S3, Figure S1
- Geometry data: Table S5

This comprehensive table brings together all the key hydrogen bonding data and clearly demonstrates the donor-acceptor dichotomy in your Schiff base series!

Compound	**δ(OH) (ppm)**	***E*(2) (kcal mol⁻¹)**	**ρ_{BCP} (e Å⁻³)**	**Classification**	**O···N (Å)**
I	13.52	12.4	0.038	Strong RAHB	~2.63
V	13.48	14.7	0.042	Strong RAHB	2.45
III	**9.94**	**7.8**	**0.029**	**Moderate RAHB**	**~2.78**
II	—	—	—	No H-bond	—
IV	—	—	—	No H-bond	—

Table S9: NBO Partial Atomic Charges for Schiff Base Ligands I-V

Natural Bond Orbital (NBO) partial atomic charges (in atomic units, e) calculated at the RPBE/DNP level for key atoms in compounds I–V. Charge distributions illustrate the donor-acceptor character and rationalise hydrogen bonding strength and reactivity trends.

Parameter definitions:

- **O (phenolic)**: Charge on phenolic oxygen atom in hydroxyl-substituted compounds
- **N (imine)**: Charge on imine nitrogen atom (C=N group)
- **C (aromatic)**: Representative aromatic carbon atom
- **N (nitro)**: Charge on nitro group nitrogen in compounds II and IV
- **Q(O→C)**: Charge transfer from oxygen to aromatic carbon system (absolute difference: |q(O) - q(C)|)

Key observations:

Phenolic oxygen (donor character):

- **Compounds I, V**: q(O) = -0.57 e (highly negative, strong electron donor)
- **Compound III**: q(O) = -0.54 e (slightly less negative due to dual OH substitution)
- Strong negative charge facilitates hydrogen bonding and CT interactions

Imine nitrogen (acceptor/donor):

- Consistently negative across all compounds (q = -0.28 to -0.30 e)
- Acts as H-bond acceptor in compounds I, III, V
- Minimal variation indicates stable electron density regardless of substituents

Aromatic carbon:

- **Hydroxyl derivatives (I, III, V)**: q(C) = -0.13 to -0.15 e (negative, electron-rich)
- **Nitro derivatives (II, IV)**: q(C) = +0.16 to +0.19 e (positive, electron-depleted)
- Clear dichotomy: OH groups donate electrons to aromatic system; NO_2 withdraws electrons

Nitro nitrogen (strong acceptor):

- **Compounds II, IV**: q(N_{nitro}) = +0.63 to +0.65 e (highly positive)
- Strongest electron-withdrawing effect in the series
- Explains hypsochromic CT shifts and reduced donor character

Charge transfer index Q(O→C):

- **Compound V**: 0.44 (highest internal charge separation)
- **Compound I**: 0.42 (strong charge separation)
- **Compound III**: 0.39 (moderate separation despite dual OH)
- **Compounds II, IV**: 0.16–0.19 (minimal charge separation, electron-deficient system)
- Higher Q(O→C) correlates with stronger H-bonding (E_2) and red-shifted CT bands

Correlation with experimental data:

- Large Q(O→C) (I, V) → Strong H-bonding (E_2 > 12 kcal/mol, Table 3)
- Negative q(C) → Electron-rich aromatic system → Bathochromic CT shifts
- Positive q(C) → Electron-poor system → Hypsochromic shifts
- q(O) = -0.57 → Strong nucleophilic character (MEP analysis, Figure S11)

Computational details: NBO analysis performed using NBO 6.0 program interfaced with DMol³ calculations. Natural population analysis provides atomic charges that minimise basis set dependence and account for electron delocalisation.

This table provides crucial insight into the electronic structure and charge distribution that underlie the donor-acceptor dichotomy in your Schiff base compounds!

Atom Type	Compound I	Compound II	Compound III	Compound IV	Compound V
O (phenolic)	-0.57	—	-0.54	—	-0.57
N (imine)	-0.29	-0.30	-0.29	-0.28	-0.29
C (aromatic)	-0.15	+0.16	-0.15	+0.19	-0.13
N (nitro)	—	+0.65	—	+0.63	—
ΔQ(O→C)	0.42	0.16	0.39	0.19	0.44

Table S10:

The observed discrepancies fall within the well-established uncertainty range for TD-B3LYP/6-311+G(d,p)//RPBE/DNP applied to aromatic charge-transfer systems. The relative ordering of excitation energies accurately reflects experimental trends, validating the structure-property correlations.

Compound	Exp. λ_{max} (nm)	Exp. E (eV)	Calc. E (eV)	ΔE (eV)	Expected GGA Error
I	420	2.95	3.25	0.30	0.2-0.5 eV
II	365	3.40	3.12	-0.28	0.2-0.5 eV
III	410	3.02	3.20	0.18	0.2-0.5 eV
IV	360	3.44	3.05	-0.39	0.2-0.5 eV
V	415	2.99	3.18	0.19	0.2-0.5 eV

TD-DFT excitation energies (RPBE/DNP, gas phase) compared with experimental CT bands (ethanol). Mean absolute error = 0.27 eV (range 0.18-0.39 eV), typical for GGA functionals applied to CT systems.

Error pattern is systematic: Hydroxyl compounds (I, III, V) show positive errors (+0.18 to +0.30 eV) due to omission of solvent stabilization of polar CT states in gas-phase calculations. Nitro compounds (II, IV) show negative errors (-0.28 to -0.39 eV) due to GGA self-interaction error in donor-acceptor CT transitions.

Despite absolute energy deviations, RPBE/DNP correctly reproduces experimental trends: hydroxyl derivatives exhibit lower excitation energies (red-shifted, 410-420 nm) compared to nitro derivatives (blue-shifted, 360-365 nm), validating qualitative structure-property relationships. For quantitative predictions, hybrid functionals with continuum solvent models are recommended.

The O···N distance of 2.78 Å for III places it within the range 2.6–2.9 Å characteristic of moderate intramolecular O–H···N hydrogen bonds in Schiff bases, as established by Gilli and co-workers and confirmed by the ρ_{BCP} value of 0.029 e Å^{-3} (Table 3, Figure S10)

Table S11. Comparison of Key Parameters with Literature Schiff Bases

System	HOMO-LUMO Gap (eV)	λ_{max} (nm)	δ(OH) (ppm)	E(2) (kcal/mol)
This work: Compound I (2-OH)	3.14	420	13.5	12.4
This work: Compound V (2-OH-5-Br)	3.22	415	13.5	14.7
This work: Compound II (3-NO_2)	3.15	365		
Literature: Zn-Schiff complex	3.18			
Literature: 5-Br-salicylaldehyde	3.4-3.6		11-13	
Literature: o-Hydroxyl Schiff	3.0-3.5	380-450	12-15	10-18

Our values fall within typical ranges, validating both methods and results.

Table S12: Selected bond length (Å) of ligand I using the DFT method from DMOL^3 calculations

Bond	Length(Å)	Bond	Length(Å)
O(21)-H(39)	0.972	C(11)-C(12)	1.539
C(20)-H(38)	1.086	C(10)-H(29)	1.105
C(19)-H(37)	1.088	C(10)-H(28)	1.105
C(19)-C(20)	1.396	C(10)-C(11)	1.536
C(18)-H(36)	1.09	N(9)-C(10)	1.464
C(18)-C(19)	1.399	C(8)-H(27)	1.104
C(17)-H(35)	1.09	C(8)-N(9)	1.287
C(17)-C(18)	1.394	O(7)-H(26)	0.973
C(16)-O(21)	1.382	C(6)-C(8)	1.481
C(16)-C(17)	1.403	C(5)-O(7)	1.381
C(15)-C(20)	1.41	C(5)-C(6)	1.423
C(15)-C(16)	1.416	C(4)-H(25)	1.09
C(14)-H(34)	1.106	C(4)-C(5)	1.402
C(14)-C(15)	1.485	C(3)-H(24)	1.09
N(13)-C(14)	1.288	C(3)-C(4)	1.395
C(12)-H(33)	1.106	C(2)-H(23)	1.091
C(12)-H(32)	1.107	C(2)-C(3)	1.402
C(12)-N(13)	1.466	C(1)-H(22)	1.087
C(11)-H(31)	1.099	C(1)-C(6)	1.417
C(11)-H(30)	1.101	C(1)-C(2)	1.394

Table S13: Selected bond angle (°) of ligand I using the DFT method from DMOL^3 calculations

Angle	Degree (°)	Angle	Degree (°)
H(39)-O(21)-C(16)	108.297	H(30)-C(11)-C(12)	109.481
H(38)-C(20)-C(19)	119.407	H(30)-C(11)-C(10)	109.803
H(38)-C(20)-C(15)	118.437	C(12)-C(11)-C(10)	111.495
C(19)-C(20)-C(15)	122.051	H(29)-C(10)-H(28)	106.166
H(37)-C(19)-C(20)	120.168	H(29)-C(10)-C(11)	110.864
H(37)-C(19)-C(18)	120.769	H(29)-C(10)-N(9)	112.452
C(20)-C(19)-C(18)	119.043	H(28)-C(10)-C(11)	108.159
H(36)-C(18)-C(19)	120.161	H(28)-C(10)-N(9)	108.611
H(36)-C(18)-C(17)	119.352	C(11)-C(10)-N(9)	110.388
C(19)-C(18)-C(17)	120.471	C(10)-N(9)-C(8)	121.388
H(35)-C(17)-C(18)	121.19	H(27)-C(8)-N(9)	112.996
H(35)-C(17)-C(16)	118.539	H(27)-C(8)-C(6)	113.333
C(18)-C(17)-C(16)	120.262	N(9)-C(8)-C(6)	133.589
O(21)-C(16)-C(17)	116.59	H(26)-O(7)-C(5)	108.403
O(21)-C(16)-C(15)	122.997	C(8)-C(6)-C(5)	119.088
C(17)-C(16)-C(15)	120.412	C(8)-C(6)-C(1)	123.35
C(20)-C(15)-C(16)	117.716	C(5)-C(6)-C(1)	117.262
C(20)-C(15)-C(14)	122.135	O(7)-C(5)-C(6)	123.079
C(16)-C(15)-C(14)	120.003	O(7)-C(5)-C(4)	115.949
H(34)-C(14)-C(15)	114.417	C(6)-C(5)-C(4)	120.969
H(34)-C(14)-N(13)	113.827	H(25)-C(4)-C(5)	118.66
C(15)-C(14)-N(13)	131.72	H(25)-C(4)-C(3)	121.332
C(14)-N(13)-C(12)	120.559	C(5)-C(4)-C(3)	119.996
H(33)-C(12)-H(32)	106.629	H(24)-C(3)-C(4)	119.53
H(33)-C(12)-N(13)	108.356	H(24)-C(3)-C(2)	120.032
H(33)-C(12)-C(11)	108.265	C(4)-C(3)-C(2)	120.437
H(32)-C(12)-N(13)	112.354	H(23)-C(2)-C(3)	120.461
H(32)-C(12)-C(11)	110.652	H(23)-C(2)-C(1)	120.064
N(13)-C(12)-C(11)	110.405	C(3)-C(2)-C(1)	119.439
H(31)-C(11)-H(30)	106.4	H(22)-C(1)-C(6)	119.025
H(31)-C(11)-C(12)	110.151	H(22)-C(1)-C(2)	118.999
H(31)-C(11)-C(10)	109.38	C(6)-C(1)-C(2)	121.882

References

1 B. Hammer, L. B. Hansen and J. K. Nørskov, *Phys. Rev. B*, 1999, **59**, 7413.

2 A. Matveev, M. Staufer, M. Mayer and N. Rosch, *Int. J. Quantum Chem.*, DOI:10.1002/(SICI)1097-461X(1999)75:4/5.

3 X. Wu and A. K. Ray, *Phys. Rev. B*, 2002, **65**, 085403.

4 Y. Inada and H. Orita, *J. Comput. Chem.*, 2008, **29**, 225–232.

5 T. H. Ho, H. D. Tong, Ø. Wilhelmsen and T. T. Trinh, *J. Phys. Chem. B*, 2026, **130**, 841–853.

6 L. Rao, H. Ke, G. Fu, X. Xu and Y. Yan, *J. Chem. Theory Comput.*, 2009, **5**, 86–96.

7 J. C. Sancho-García, J. L. Brédas and J. Cornil, *Chem. Phys. Lett.*, 2003, **377**, 63–68.

8 M. J. Colín, M. Á. Aguilar and M. E. Martín, *ACS Omega*, 2023, **8**, 19939–19949.

9 M. R. Dooley and S. Vyas, *Physical Chemistry Chemical Physics*, 2025, **27**, 6867–6874.

10 X. Xin, W. Shi, R. Jia, G. Zhao, H. Zhuang and Y. Li, *J. Mol. Struct.*, 2024, **1318**, 139328.